Bar-Ilan University

Dendritic Flux Avalanches in Superconducting Hybrid Structures Exposed to Fast Ramping Magnetic Fields

Michal Wasserman

Submitted in partial fulfillment of the requirements for the Master's Degree in the Department of Physics, Bar-Ilan University

Ramat-Gan, Israel 2023

This work was carried out under the supervision of Prof. Yosef Yeshurun

Department of Physics, Bar-Ilan University.

Acknowledgments

This work would not have been possible if not for the extensive help and support of numerous people that I would like to thank deeply and acknowledge here.

First of all, I am truly grateful for my advisor, Prof. Yosi Yeshurun, for giving me the opportunity to work and research in his lab, and for his professional and caring guidance and endless patience. I am also thankful for the invaluable life lessons I had the privilege to learn from him, and which I am still working to adopt myself.

I am also very grateful for Prof. Avner Shaulov for the many intelligent and enriching discussions he offered, for his support, and for his wise and creative ideas. He was sure of the possibility of surface and hybrid dendrites far earlier before I was ready to consider it.

I would like to acknowledge and give my thanks for Prof. Amos Sharoni and his research group as well. Without their help with the fabrication of the samples, this work would not have been possible.

I would also like to give my thanks for Prof. Michael Baziljevich. Even though his visits in the lab were few and short, the amount of knowledge he offered during those visits was enormous.

Next, I would like to acknowledge and give my thanks for the rest of my colleagues and seniors in Prof. Yosi Yeshurun's research group: For Dr. Shuki Wolfus, who was always ready with a helping hand for any question and request. For Jonathan Shvartzberg, his help during my first steps into the superconducting subject and the training he provided on the fast MOI system. For Eli Perel, for fixing the MOI system patiently, and unfortunately, repeatedly. I would also like to thank Zoharchan Sofer, Ofek Marelly and Arial Roitman for their helpful discussions, advice and support. And lastly, I would like to thank Itay Garofy and Dr. Yasha Niculshin, for helping me with the simulations presented in this thesis.

I would like to give my thanks for the physics department in Bar-Ilan university as well. Rita Dadiomov is especially a force to be reckoned with, and together with Dr. Yossi Ben-Zion and the rest of the administrative Staff, I never remained with unsolved problems.

I would also like to give my honest thanks for my close friends, Noam, Leah and Nechama, for helping and supporting me from outside the academia, while understanding little of the physical nonsense I talked about. I truly appreciate you being there for me.

And lastly, I am truly thankful for my family, for accompanying me along this path. For my parents, with their useful advice and endless assistance, and for my siblings. Specifically, I would like to give my thanks for my sister and her personalized memes, which were weirdly effective and helpful.

Thank you all.

Contents

Abstract

Type-II thin-film superconductors exposed to magnetic field often exhibit magnetic instabilities in the form of dendritic flux avalanches, where abrupt bursts of magnetic flux invade the superconductor in narrow regions, forming dendritic structures. These avalanches occur below a threshold temperature, T_{th}, and between a temperature-dependent lower and upper threshold fields, H_{th}^{1} and H_{th}^{2}, respectively. As the magnetic instability can have a catastrophic effect on the performance of superconducting applications (raising the local temperature well above T_c and, in some cases, even leaving permanent damages), it is essential to study methods to prevent the occurrence of such avalanche events and to increase the superconducting stable regime. Recent experiments, exploiting slow magneto-optical imaging (MOI), demonstrated suppression of the dendritic avalanches by coating the superconducting films with additional conducting layer; either normal-conducting or superconducting. These MOI experiments, however, were limited to imaging of avalanches generated by slow ramping magnetic fields of ~1 mT/s.

As was demonstrated in a previous work in our lab, with increasing ramping rate of the magnetic field, avalanches appear at higher temperatures above the threshold temperature and at a wider range of applied magnetic fields, increasing the magnetic instability regime dramatically, and harming superconducting applications even further. Thus, studying the efficiency of possible suppression methods, such as the conducting-coating method, under fast ramping fields as well, is strongly necessary. However, experiments that examine the effect of such coating methods on dendritic avalanches generated during fast field ramp are still lacking.

In this work, we exploited the unique fast MOI system in our lab, which allows the measurements of dendritic avalanches generated by ultra-fast ramping fields, for the study of the mentioned coating method avalanches' suppression in superconducting samples partially coated with either normal conductor or superconductor coat layer, under fast ramping rates. Therefore, this dissertation focusses on two different sets of experiments, each constructed to investigate the flux avalanches' suppression in a different hybrid structure.

The first set investigates the flux avalanches' suppression in partially metal-coated superconducting samples, specifically a partially Cu-coated NbN film, by observing the partial coat layer effect on the advancing dendritic avalanches through MO images and by measuring the

dependency of the avalanches' lower threshold field, H_{th}^{1}, on the field ramping rate, $\dot{H}$. MO images show the partial metal coat layer suppresses completely, at all the measured ramping rates, avalanche nucleation along the coated edges, due to the damping of vortex motion by induced eddy currents in the Cu coat layer. The images also show that at low ramping rates the Cu coat stops most advancing dendritic branches at the coat boundary, the only few crossing branches are stopped shortly after by electromagnetic braking of the eddy currents. With increasing ramping rate, however, the sample suffers more energetic avalanches the induced eddy currents are insufficient to suppress, thus more branches manage to overcome the electromagnetic braking, penetrate the metal-coated area and advance deeper into it before stopping completely. Still, as the lower threshold fields of the Cu-coated sample are higher than the threshold field of the bare sample at all the measured ramping rates, the Cu-coat increases the magnetic stability of the entire sample and offers a good suppression method, with better efficiency at slow ramping rates of $\sim 0.1\ kT/s$ than at higher ramping rates.

In the second set of experiments, we investigated the flux avalanches' suppression in superconducting partially coated hybrid samples, specifically a partial Nb-coated NbN film, by observing the partial coat layer effect on the dendritic avalanches through MO images and by measuring the threshold field's, H_{th}^{1}, dependency on both temperature and field ramping rate, $\dot{H}$. MO images show that, unlike in the case for the Cu-coated sample, dendrites in the superconductor-coated superconducting sample nucleate along both the uncoated and coated edges of the samples. However, the threshold fields and threshold ramping rates of the coated edge are higher than the uncoated edge's due to the increase of the effective thickness and the additional shielding currents in the coated area. The images also show that all dendritic branches that reach the coat boundary are stopped completely and abruptly, only managing to penetrate the coated area above a threshold field and a threshold ramping rate, higher than the threshold values of both the coated and uncoated areas. The threshold fields of all areas, however, still decrease with increasing ramping rate, as the fast-ramping field induced more energetic avalanches the superconducting shielding currents are insufficient to suppress.

Comparing the two coating methods, we see, quite surprisingly, that the superconductor-coated superconducting samples exhibiting significantly higher threshold fields than the metal-coated samples under fast ramping fields. Meaning that the Meissner shielding currents and the increased effective thickness of the superconducting hybrid structure offer a more efficient suppression mechanism than the avalanches' suppression by eddy currents induced in the metal coat layer, even at fast ramping fields.

Since flux entry (either stable or unstable) in hybrid, partially superconductor-coated superconducting samples have not been studied much, we conducted a more extensive study of these samples and investigated the effect of slow ramping fields on the dendritic avalanches as well as fast ramping fields. From these extensive measurements, we present experimental evidence for the surprising existence of two new and distinctive types of dendrites: Hybrid dendrites, that occupy both of the different superconducting layers of the hybrid structure, and are affected by both. And surface dendrites, that are created at the coat layer only, and not in the superconducting underlayer. Each of the new types of dendrites has its unique characterization and behavior, as is seen through their spatial dendritic shape and temperature dependency; the hybrid dendrites show a dendritic formation that is affected by both Nb and NbN layers and weak temperature dependency, while the surface dendrites show stronger sensitivity for temperature variations, due to their creation in the Nb coat layer with its lower critical temperature.

1. Introduction

1.1. Thermo-magnetic instabilities

In an ideal type-II superconductor in the mixed state, the repulsion between vortices leads to the formation of an Abrikosov lattice [1]. In real superconductors, however, local defects act as pinning centers and disrupt the vortex lattice. Under the influence of electrical currents (transport or Meissner screening currents [2]) the vortices are also affected by the Lorentz force $F_L = j \times \Phi_0$, j being the current density and $\Phi_0 = h/2e$ being the flux quanta of a single vortex. In the case where the Lorentz force exceeds the pinning one, vortices are released and move through the superconducting sample, dissipating local Joule heating at a rate of $j_c E$ in their path [3]; j_c being the sample's critical current density, and E the local electrical field. The competition between the pinning and Lorentz forces give rise to a metastable state of inhomogeneous distributed flux described by the Bean critical state [4], where the vortices density decreases from the sample's edges inwards with slope of $\mu_0 j_c(T, B)$, as can be seen in figure 1.1.1a below.

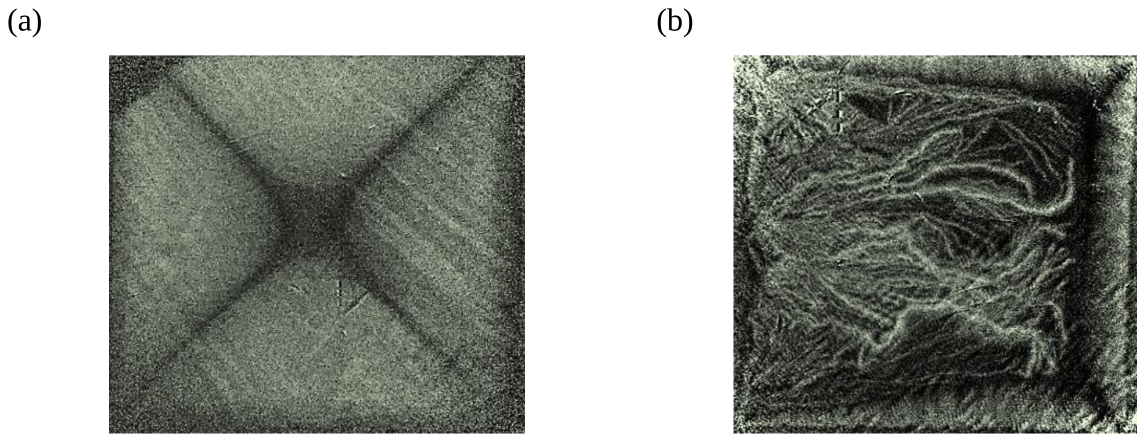

Figure 1.1.1: Magneto-optical images of flux penetration in 300 nm thick NbN films at $5.5K$. a) Smooth flux penetration at magnetic field of $5.5\ mT$ and ramping rate of $0.6\ kT/S$. b) Positive dendritic flux avalanche at $5\ mT$ and ramping rate $0.4\ kT/S$.

The equilibrium between the Lorentz and pinning forces is delicate, thus even small variations in temperature or magnetic field can release some pinned vortices to move; this motion by itself is slow and is referred to as 'flux creep' [5,6]. A much faster dynamic can occur if the local Joule heating, caused by the released flux motion, increase the local temperature and causes further vortices depinning, their motion inducing even further heating. In this case, where the sample's heat diffusion is insufficient to overcome the competing magnetic flux diffusion, the described positive feedback loop leads to a large-scale thermomagnetic instability (TMI) that harms the critical state. In thin-film samples, those instabilities take the form of abrupt dendritic flux avalanches [2], as can be seen in figure 1.1.1b above.

Studies of dendritic avalanches over a wide range of superconducting materials show the instabilities occur below a threshold temperature $T_{th} < T_c$, and between threshold magnetic fields $H_1^{th}(T)$ and $H_2^{th}(T)$ which merge at T_{th}, as can be seen in figure 1.1.2a. Inside this unstable regime, the number, size, branching degree and overall shape of the dendritic avalanches all vary with both temperature and field.

This dendritic behavior is described by the coupled Maxwell and thermal conduction equations, the resulting model being referred to as the thermomagnetic model [7]. Using this model, the turning point where the magnetic diffusion overpowers the thermal diffusion and introduce the first dendritic avalanche, occurs as the flux penetration depth reach a threshold depth, l^*, expressed by:

$$(1) \qquad l^* = \frac{\pi}{2}\sqrt{\frac{\kappa}{|j_c'|E}}\left(1-\sqrt{\frac{2h_0}{nd|j_c'|E}}\right)^{-1}$$

κ being the sample's thermal conductivity, j_c' the temperature derivative of the critical current, E the electrical field, h_0 the heat transfer between the superconducting sample and its substrate, n the exponent for the sample's power-law relation $E \propto j^n$ and d being the sample's thickness. By also considering Bean's model for thin type-II films in perpendicular magnetic field H, and the dependency it introduced for the flux penetration depth l on the external field H, as derived in [8], the lower threshold field can be extracted from:

$$(2) \qquad H_1^{th} = \frac{j_C d}{\pi}\,\mathrm{arccosh}\left(\frac{w}{w-l^*}\right),$$

w being the film half-width and l^* being the j_C-dependent threshold flux penetration depth given in equation (1). The upper threshold field H_2^{th}, according to the thermomagnetic model, corresponds to the flux penetration depth reaching the sample's half-width, where $l = w$, while the threshold temperature, T_{th}, corresponds to $l^* = w$, where the threshold fields merge with each other and the sample is stable for all applied fields.

As can be seen from the explicit dependency of the threshold flux penetration depth and fields on the sample's critical current density, j_c, its effect on the sample's thermomagnetic instability is huge and in fact can also serve as a measure for the system's resistance against flux entry. The existence of the two threshold fields can therefore be understood by taking into account the behavior of j_c with the external field H; at low fields, j_c is high and the system strongly resists the entrance of magnetic flux. However, as H increases, j_c decreases and some flux starts entering the sample. Above some lower threshold value H_1^{th}, as j_c is low enough to allow partial flux entry but still strong enough to struggle against it, the flux enters in the form of unstable rapid dendritic avalanches. The instability remains as the external field H increases further, until it exceeds some upper threshold value H_2^{th} at which j_c decreases enough to no longer resist the entrance of the flux, and so it enters in a smooth fashion once again and the sample regains its stability. By finding the sample's exact $j_c(H)$ and $H_{th}(j_c)$ relations and their intersection points, the threshold fields H_1^{th} and H_2^{th} can be found, as presented schematically in figure 1.1.2b. It is worth noting that the critical current, j_c, may be slightly different for increasing and decreasing fields, resulting in different threshold fields for positive flux and anti-flux avalanches [9].

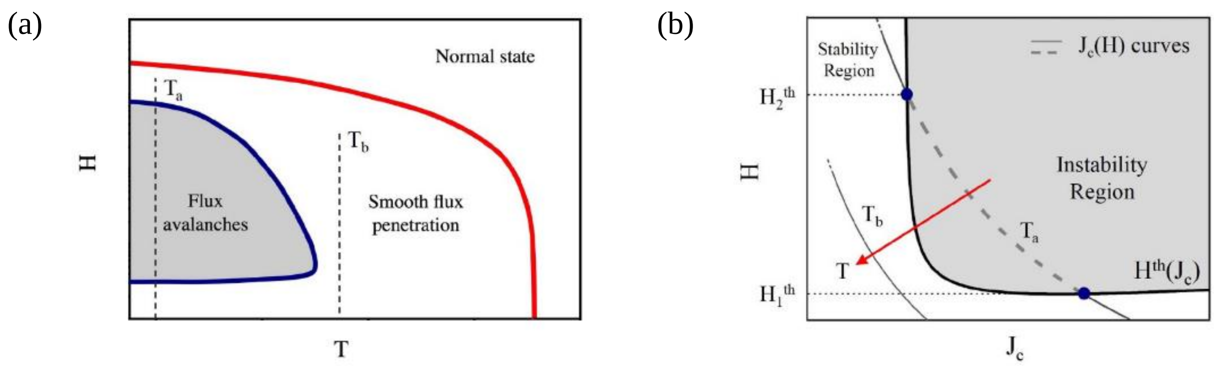

Figure 1.1.2: a) schematic H versus T diagram. Flux avalanches occur within the unstable regime defined by $T < T_{th}$, $H_{th}^1 < H < H_{th}^2$. Outside of the unstable regime the flux penetrates smoothly according to the critical state model. b) schematic H versus J_C diagram, based on the thermomagnetic model. The intersection of the $H_{th}(j_C)$ and the $j_C(H)$ curves give the threshold fields of the instability regime. For $T > T_{th}$ the curves do not intersect and the sample is stable for all fields. [10]

Though the dendrites formation is a stochastic process [7], the dendrites tend to nucleate at indents at the sample edges, where high electrical fields are present [11], and propagate towards the sample's center. Closely after their nucleation, the avalanches advance in extremely high velocities that are linearly proportional to the magnetic field and can reach values up to $180\,\frac{km}{s}$, later slowing down to lower and approximately constant velocities, until stopping in their way towards the sample's center [12,13].

1.1.1. Effect of field ramping rate

Although the unstable regime is usually described by the threshold temperature T_{th} and fields H_1^{th}, H_2^{th}, the magnetic field's rising rate $\dot{H}_a$ also has a significant role in the appearance of the dendritic avalanches. In fact, high-T_C superconductors, such as YBCO, are stable under slow ramping rates and only exhibit dendritic avalanches under extreme conditions, such as an extremely high field ramping rates [14]. Fast rising magnetic fields cause higher electrical fields, so that moving flux generates larger amounts of Joule heat in its path and thus enhance even further the magnetic instability [15–18]. With increasing magnetic field's ramp rate, the dendritic avalanches appear at higher temperatures above T_{th} and for a wider range of magnetic fields, in the previously stable regime.

By expanding the thermomagnetic model to include the electrical field dependency on the magnetic field ramping rate in the case of thin rectangular film under perpendicular field, as derived in [19], the dependency of the threshold fields on the magnetic field's ramp rate can be described [20]. The threshold fields are strongly affected by the heat removal of the sample, thus, for small applied magnetic fields, when the heat introduced by the flux motion is still relatively small and the main heat removal mechanism is through lateral heat diffusion in the sample, the threshold fields are determined by the following expression:

$$(3) \qquad H_{th,\kappa} = \frac{d j_C}{\pi}\left(\frac{\pi^2 \kappa T^*}{n w^3 j_C \mu_0 \dot{H}_a}\right)^{\frac{1}{5}}$$

Where κ is the superconductor thermal conductivity, n is the sample's creep exponent and $T^* = |\partial \ln j_C / \partial T|^{-1}$. At higher fields, however, when the heat generated by the moving flux is greater and the dominating heat removal mechanism becomes the heat removal by the substrate, the threshold fields are expressed by:

$$(4) \qquad H_{th} = \frac{d j_C}{\pi} \operatorname{atanh}\left(\frac{h T^*}{n w d j_C \mu_0 \dot{H}_a}\right)$$

where h is the heat transfer coefficient to the substrate. Below a certain minimal ramp rate $\dot{H}_a^{min} = hT^*/nwdj_C\mu_0$, relation (4) gives no solutions, and the sample is stable for all applied fields and no dendrites occur. Only above this minimal ramp rate there exist two solutions, corresponding to the upper and lower threshold fields.

With increasing field ramping rate, the threshold fields move further away from each other, resulting in increasing unstable regime. In particular, by using Kim's model [21] so that $j_C = j_{C0}/(1 + H_a/H_0)$, H_a being the externally applied field and H_0 being a sample-dependent characteristic field, the upper threshold field H_2^{th} shows linear dependency on the rising rate, expressed by [15] :

$$(5) \quad H_2^{th} = \frac{nwdj_{C0}\mu_0 H_0}{hT^*}\dot{H}_a - H_0.$$

Almost all research works on the dendritic avalanches and magnetic instabilities have been done under slow rising field rates, typically $\sim 1\ mT/s$, exploiting slow magneto-optical imaging (MOI) of the vortex system at a rate of 25 frames per second (fps) [7,9,12,13,23]. Notable exceptions are works published by our group that developed a unique MOI system which allows imaging at a rate of up to 70, 000 fps and a fast field rise of up to 3 kT/s [23]. The MOI techniques and the features of our unique system will be described in details in the Research Methods Section below.

1.2. Suppression of thermomagnetic instabilities

As the magnetic instability can have a catastrophic effect on the performance of superconducting applications (raising the local temperature well above T_c and, in some cases, even leaving permanent damages [14]), it is essential to discover ways to prevent the occurrence of such avalanches and to increase the stable regime. All while trying to keep the desired properties of the superconductor itself. A possible way is the coating of the superconductor film by an additional conducting layer, either a normal-metal or a superconductor layer.

1.2.1. Metal coating

The suppression of the flux avalanches by a normal-metal coating layer was first described in [24], where a MgB_2 film was partially covered by an Al foil. Later works [25–31] repeated the results for different sets of coating metals and superconductors films both for completely coated samples and for partially coated samples. In all these works, at temperatures above T_{th} the sample is in its stable regime and the flux smoothly penetrates both the coated and uncoated regions.

However, below T_{th}, as the sample enters the instability regime, the coated regions showed significant suppression of both avalanches' nucleation and progression, while the uncoated regions still suffered from magnetic instabilities.

The suppression was initially assumed to be caused by the normal-metal layer behaving as a heat-sink, thus thermally stabilizing the superconductor and preventing flux avalanches [24]. However, Colauto *et al.* [31] later proved that the suppression happens even without thermal contact between the layers. Instead, the suppression is explained by electromagnetic braking due to eddy currents generated in the metallic layer by the fast propagating vortices [29,33,34]. The thicker and better conductive the coating layer is, the larger the generated eddy currents are and the better the sample's avalanches' suppression is [26,35]. Specifically, Vestgården *et al.* [33] defined a dimensionless braking parameter for coated samples:

$$(6) \qquad S \equiv \frac{d_m \sigma_m}{d_s \sigma_{sn}},$$

where d_m, σ_m are the metal layer's thickness and conductivity, and d_s, σ_{sn} are the superconductor's thickness and its normal-state conductivity. Large S values, such that $S \gg 1$, correspond to large braking effect and efficient flux suppression. Another parameter to influence the electromagnetic braking is the avalanches' velocity, where faster avalanches induce larger eddy currents and therefore cause stronger suppression [28] .

Finally, an additional suppression mechanism considered by Brisbois *et al.* [28] and Albrecht *et al.* [29] is the repulsion of propagating avalanches by vortices accumulated at the metal-coating interface due to the velocity difference between the coated and uncoated regions.

1.2.2. Superconducting coating

Suppression effect can also be achieved by coating the superconducting sample by different superconducting layers [35], or equivalently by step-increasing the superconductor's thickness [25]. Like the metal-coated samples, those superconductor-coated samples exhibit efficient flux avalanches' suppression in the unstable regime. However, the superconductor-coated samples also show suppression of smooth flux penetration in the stable regime.

The suppression of homogenous superconducting samples with step in thickness can be explained by considering the dependency of the thermomagnetic instability on the sample thickness. such subject was studied by Baruch-El *et al.* [36] with uniform YBCO films of different thicknesses, where he showed the thermomagnetic instability shrinking with increasing thickness, but attributed it to the increase of the critical current density j_C and to the increasing number of pinning centers with the increasing sample's thickness.

In order to specifically treat the partial coating of a sample, however, and not just an homogenous coated sample, one can treat the superconductor coating layer as a perfect metal, like Brisbois *et al.* [28] does to explains the suppression of samples with step-increased thickness. Like the suppression in the metal-coated case, here too the avalanches are stopped by electromagnetic braking due to generation of eddy currents. Because of the superconductor infinite conductivity, even slow propagating vortices, *i.e.*, smooth flux penetration, generate screening/eddy currents in the coating layer, that suppress the flux advancement. However, such explanation should be considered with caution, since treating the superconductor as simply a perfect conductor and neglecting its special behavior can be very problematic. Layered and complex superconducting structures are more complicated than the simple superposition of the individuals superconducting layers they consist of, as can be seen in [38,39] , where 3D shifted strip arrays of isolated, stacked and partially overlapping superconducting layers were fabrication and studied for smooth and unstable flux penetration. One interesting and unexpected result such structures show is dendritic avalanches "advancing" along overlapping layers due to enhanced magnetization effects, though each is isolated one from the other.

Pinheiro *et al.* [35], on the other hand, considered the case of suppression in hybrid superconducting samples of different materials and explained the suppression by proximity effect between the two different thin layers of the Nb/NbN bilayer structure in their work. The stable Nb layer stabilizes the unstable NbN layer, while keeping the NbN preferable properties such as its high T_C and j_C. Such Nb/NbN hybrid structures were also studied by other research groups as a way to stabilize the superconducting NbN sample against thermomagnetic instabilities and in order to enhance its performance, though in different geometries than of a thin rectangular film [39], [40]. Specifically, Vasiliev *et al.* [41] showed that instabilities suppression is optimal when the coating layer is of lower critical current density and of optimal thickness.

Overall, the coating of superconducting samples by conductive layers proposes a good method for dendritic avalanches' suppression under slow rising magnetic fields, for which it was measured, although questions regarding the underlying mechanism of the suppression remain open, especially in the superconductor bilayer case. Furthermore, the suppression ability and behavior of such structures against fast ramping rates is still completely unknown, as no research on such structures could previously be done under this condition. Since faster rising fields increase the superconductor's magnetic instability, the suppression ability of such structures might and is expected to change with the sweeping rate. As mentioned above, our unique experimental setup allows, for the first time, such a study and will be used here for such measurements.

Although the suppression of metal-coated sample was studied extensively, in all of the mentioned cases, the external magnetic field ramping rate was slow, around $\sim 1\ mT/s$ and no works were done on fast ramping fields. Since the metal coat layer and the superconducting underlayer are expected to have opposing reactions to the magnetic field ramp rate, the study of such metal-coated samples is required, in order to determine the overall response. The metal coat is expected to resist the flux advancement to a stronger degree with increasing external field ramping rate and increased induced eddy currents, and with increasing dendrites velocity. While the superconductor underlayer, on the other hand, is expected to become even more unstable as the field ramping rate increases, and to suffer even more of dendritic avalanches. By measuring a metal-coated sample against increasing ramping rate we study whether the coated sample suppression is enhanced with increasing ramping rate, whether the sample thermomagnetic instability worsen and it suffer avalanches to even higher degree, or whether the suppression will show some nonmonotonic behavior where there is an optimal ramping rate at which the suppression is maximal.

Similarly, considering the response a superconductor-coated superconductor might have with increasing ramping rates, we can expect to see a similar response as a single layer superconductor. Since both layers have individually the same dependence on the ramping rate, we can expect to see the same overall behavior for a bilayer sample as well. however, as we mentioned, superconducting complex structures can have different behavior to that of each layer individually. Specifically, by measuring a partially coated hybrid structure of different superconductors, we hope to study closely the dendrites of each area and see the behavior of the boundary between the areas.

2. Experimental setup

2.1. Samples fabrication

The following section is dedicated for the description of the samples made throughout the work, and the fabrication processes each went under to enable the measurements of the desired experiments. In order to allow easy identification of the discussed samples, we use uppercase letters (A, B and C) to identify the sample and an additional roman numeral subscript (A_{I}, A_{II}, A_{III} etc.) to describe their specific fabrication stage.

As the dendritic avalanches phenomenon is mostly observed at low-temperature thin superconductors films, we chose to focus our efforts with such samples. Particularly, we chose to use NbN thin films as the base superconducting layer of our samples, above which we will deposit additional coating layers of a similar thickness (either metallic or superconducting). NbN is a promising low-temperature superconductor with relatively high critical temperature T_C and current density j_C, making it suitable for many superconducting applications [32]. However, it is also prone to magnetic instabilities over a large portion of its superconducting phase, making it an ideal material to use in this work for the research of dendritic avalanches.

Samples of bare $300\ nm$ thick NbN were sputtered on $8mm \times 8mm$ sapphire substrates, using an AJA DC reactive magnetron sputtering system, by the research group of Prof. Amos Sharoni. From R vs T measurements done using Quantum Design's PPMS, the samples showed a sharp phase transition around $T_C = 13.7\ K$. In order to tailor the sample's instability regime[1] to the limitations of our experimental setup (as will be described in greater detail later) the samples' size was reduced before further measurements and additional fabrication steps. Here, however, the fabrication process varies slightly between the different samples.

The first sample, sample A, was cut down mechanically to a size of $4.5\ mm \times 3.8\ mm$, using a diamond tipped cutter[2], resulting in the bare NbN sample[3] A_I described in figure 2.1.1a

[1] The $8mm \times 8mm$ sized samples suffered an extremely large instability regime, dendritic avalanches occurring over a very wide range of magnetic fields, even at low ramping rates of $\sim 0.2\ mT/s$, and even at temperatures close to the critical temperature. In order to slightly stabilize the samples, we had to reduce their area size.

[2] Due to the sample's still relatively small size, photolithographic processes proved to be slightly problematic.

[3] A convention we will keep throughout this work to avoid confusion is the distinction between the term "bare sample" for the NbN samples before any coating step, "uncoated area" to describe the areas of uncovered NbN in samples after they went under a coating process, and the term "coated area" to describe the areas of covered NbN in samples after they were coated.

below. A partial Cu coating of 150 nm was later sputtered on the sample, using a Bestec sputter deposition system by Moshe Feldberg from Bar-Ilan's nano-center, resulting in the coated sample A_{II}, as described in 2.1.1c. The sample was then coated again with additional 300 nm Cu, resulting in sample A_{III}, as described in 2.1.1d

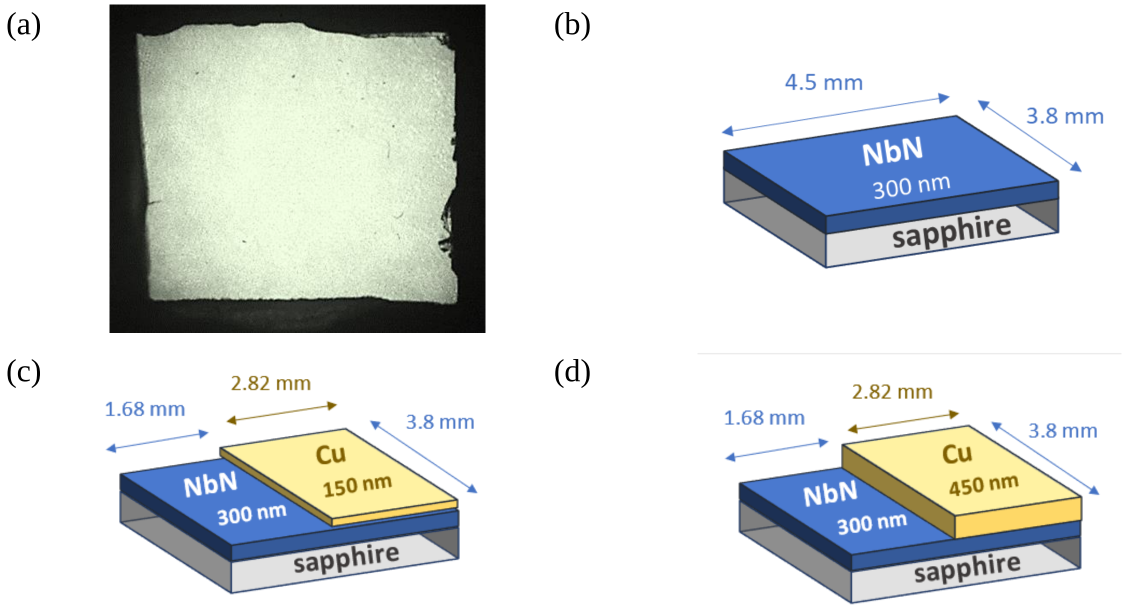

Figure 2.1.1: a) Optical image of the initial sample A_I. The sample has many indents, caused by the cutting, which help the nucleation of dendritic flux avalanches in the sample. b) A schematic of the bare sample A_I. c) A schematic of the 150 nm Cu-coated sample A_{II}. d) A schematic of the 450 nm Cu-coated sample A_{III}.

For the superconductor-coated superconducting samples, we chose the coating layer to be of Nb. Though the Nb has lower critical temperature and critical current density than the NbN, it is quite stable against dendritic flux avalanches, and is easy to work with as a coating layer to the NbN, the combination studied in previous works [35] . By having a lower critical temperature than the NbN underlayer, we can also observe the behavior of the sample at the temperature range where the Nb becomes normally conductive while the NbN underlayer is still superconducting.

Bare samples, B_I and C_I, were etched using Reactive Ion Etching (RIE) and lithography processes, as is shown in figure 2.1.2a. the samples were then partially coated by coating layer of $300\ nm$ and 450 nm thick Nb, sputtered using an AJA DC reactive magnetron sputtering system, in Prof. Amos Sharoni's lab.

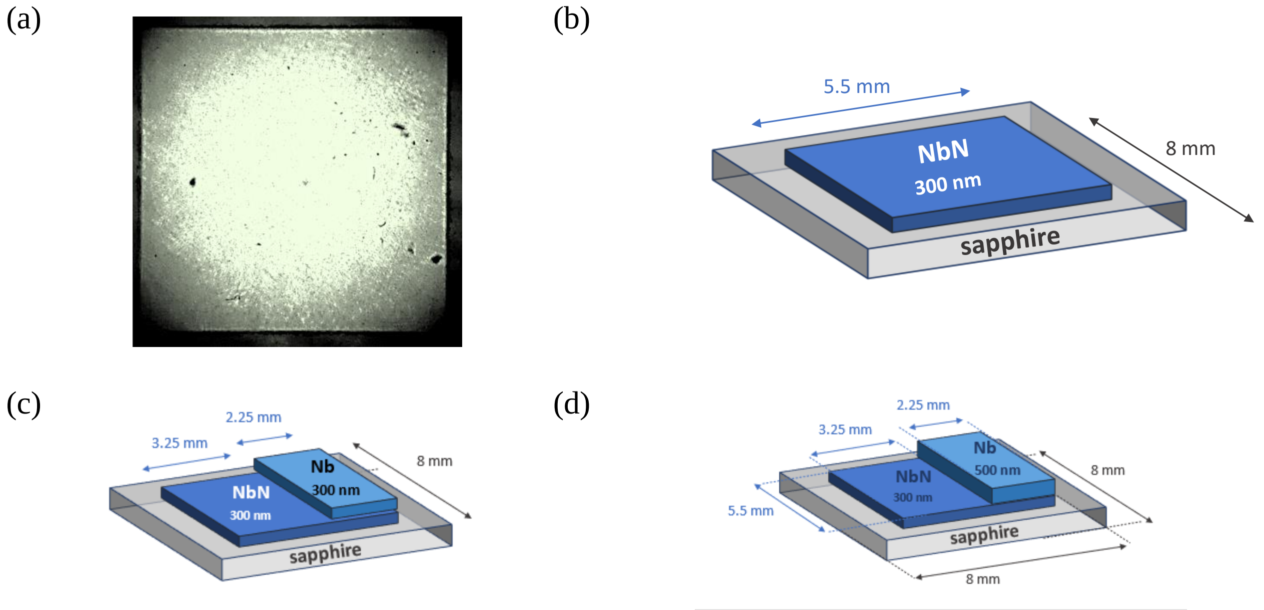

Figure 2.1.2: a) representative optical image of the initial sample C_{I} (sample B_{I} looking the same). In contrast to sample A used for the metal coating (see Figure 2.1.1), here we etched the sample, resulting in a much smoother perimeter. b) A schematic of the bare samples B_{I} and C_{I}. c) A schematic of the 300 nm Nb-coated sample B_{II}. d) A schematic of the 450 nm Nb-coated sample C_{II}.

The different samples, with the specification of their layers, are organized in table 2.1.3 below, for a better clarity.

Metal coating		
Bare 300 nm NbN	300 nm NbN + 150 nm Cu	300 nm NbN + 450 nm Cu
Sample A_{I}	Sample A_{II}	Sample A_{III}

Superconductor coating		
Bare 300 nm NbN	300 nm NbN + 300 nm Nb	300 nm NbN + 450 nm Nb
Sample B_{I}	Sample B_{II}	--
Sample C_{I}	--	Sample C_{II}

Table 2.1.3: Summary of the different measured samples' names and description.

2.2. The MO system

One of the strongest tools for the measurement of flux avalanches, which will be used throughout this work, is the magneto-optical imaging method (MOI). The MOI is a microscopy technique based on the Faraday effect, where the polarization plane of propagating light undergoes a rotation of:

$$(1)\ \beta = \nu B d$$

in a transparent dielectric medium (referred to as an indicator), where β is the polarization's rotation angle, ν is the wavelength-dependent Verdet constant of the indicator material, B is the magnetic field parallel to the light's propagation and d is the indicator's thickness, as demonstrated in figure 2.2.1a). Employing this phenomenon with a polarized microscope, the spatial magnetic flux distribution of a sample can be optically observed by placing an indicator on top of it, as is shown in figure 2.2.1b). In order to achieve significant rotation angles we use a Bi:YIG indicator that exhibits in-plane magnetization and very strong Faraday effect, grown on a gadolinium gallium garnet (GGG) substrate. By also coating the indicator's bottom with a reflecting Al layer, the light goes through the indicator twice, thus multiplying the indicator's effective thickness and enhancing the rotation angle even further. It is important to note here, however, that although the MOI is considered a noninvasive method, in the case of superconducting measured sample the indicator's Al layer can act as a metallic coating layer to the sample and suppress dendritic flux avalanches, as was discussed in the introduction section above, and thus affect our measurements [31]. Yet, as the thickness of the metallic layer is of order of 100 nm, we do not expect a significant effect on the MOI images.

(a) (b)

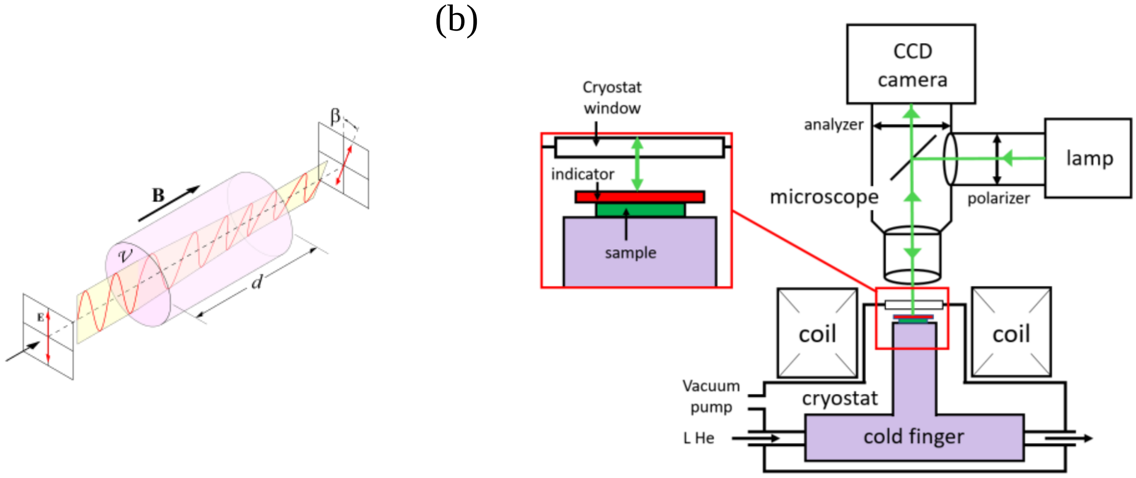

Figure 2.2.1: a) An illustration of the Faraday effect in an indicator medium. b) A typical schematic of MOI set up. The sample is mounted on top of the cryostat's cold finger and the indicator film is placed on top of the sample. A coil placed around the sample chamber is used to apply magnetic fields. Light from external source is polarized at the microscope entrance by a polarizer and is reflected towards the indicator. The light polarization is rotated according to local magnetic fields in the indicator. Then, the Faraday-rotated light is reflected back to a second polarizer, known as an analyzer, placed at approximately 90° angle in relation to the first polarizer so that only the rotated component of the light pass through. Finally, an image of the flux distribution in the sample can be observed by the camera, where bright regions of the image correspond to regions of high magnetic flux, and dark regions correspond to low magnetic flux.

Since in this research we are measuring the properties of superconducting samples in their superconductor phase, below their critical temperatures T_c, another essential part of the MOI system is of course its cooling setup. Here we use a continues flow Microstat He based cryostat, custom made by Oxford Instruments to allow the MOI measurements even under fast varying fields (as is further elaborated in the section below), and an Oxford ITC instrument for the temperature control and measurement.

All throughout this work, the MOI measurements were made post zero-field cooling (ZFC) of the sample; The superconducting sample was heated to above the sample's critical temperature, T_c, to release any remnant magnetic flux that might have been trapped in the sample. Then it was cooled again to the desired target temperature under zero external magnetic field to allow the measurement of the sample under idle conditions. It should be mentioned in this regard, that repeated heating and cooling of the cryostat chamber for prolonged periods of time can cause small mechanical vibrations and movement between the cold finger, the mounted sample, and the indicator above it. As a result, two problems can occur; The first is the variation of the thermal coupling between the cold finger and the sample. Since the threshold values of the sample's unstable regime are dependent on the sample's temperature and its thermal coupling, such vibrations can affect the results we achieve and add to the noise in our results. The second problem is the indicator, with its metallic Al bottom layer, getting closer to the sample during the experiment and enhancing the suppression of the flux avalanches in the sample [31]. From a few checks we did on our system we could indeed detect such a variation of threshold results during long measurements. Unfortunately, as such MOI measurements are long by nature, there was no way to escape such those problems but to take the added noise of the results into consideration.

2.3. The fast-switching system

In order to allow microsecond MOI measurements under fast rising magnetic fields, several significant modifications on the conventional setup presented in the previous section were made; (a) We use a Phantom V210 high speed camera from Vision Research with recording speed as high as 70,000 frames per second (fps) rather than the conventional slow, video-rate (25 fps) camera. (b) The camara's short acquisition time demands a powerful light source, for which a powerful Nd:YVO4 Q-switched laser source is used. (c) In order to suppress any eddy currents that will oppose the fast-rising magnetic fields, the cryostat metallic parts were modified as well. The copper cold finger was replaced with a sapphire rod, the sample chamber's cover was made of PEEK plastic and the radiation shield was produced with two slits along its height in order to suppress any induced currents around the sample. (d) In order to apply the fast-ramping magnetic fields we use a specially designed coils system and power supply, as presented in figure 2.3.1, Large amounts of electric energy are stored in an auxiliary coil with very high inductance. Once charged, the energy in the storage coil is discharged towards a much smaller coil around the sample, with a rate determined by the inductance ratio and a controlled voltage limit on the storage coil. More details are described in reference [23].

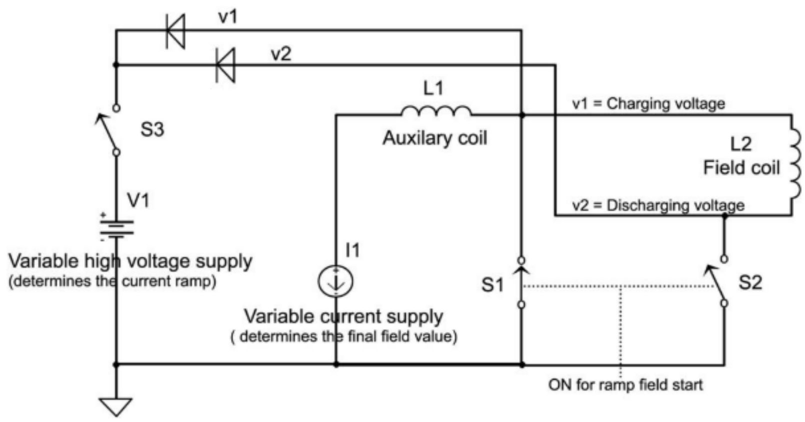

Figure 2.3.1: circuit diagram of the high-speed switch for the twin coil system. The current power supply I1 feeds the auxiliary pump coil L1 while the field coil L2 stays disconnected. When the S2 electronic switch is activated (and S1 disconnects simultaneously) voltage starts to build up over L1 to a maximum limit. This voltage produces a current through L1 at rate of V/L. The voltage limit is controlled either by an internal voltage limiter (fixed value) in the circuit, or by connecting the variable high voltage supply V1 (trough switch S3). This allows the applied field ramp rate to be varied. Fast insulated gate bipolar transistor (IGBT) switches are used for S1 and S2.

However, although the coil system enables a wide range of applied magnetic fields and the measurement of high and varying ramp rates, there is a tradeoff. The system is partially limited in its measurement values, the possible ramping rates and applied magnetic fields dependent on each other, as is shown in figure 2.3.2. Low magnetic fields are particularly restricted only to relatively low ramping rates, while high fields can be measured over a much wider range of ramping rates. Those limitations strongly restrict the measurements and characterization of the dendritic flux avalanches across the H vs $\dot{H}$ plane, especially for low applied magnetic fields, a restriction that will be reflected in some of our results, as will be seen later, in the results section.

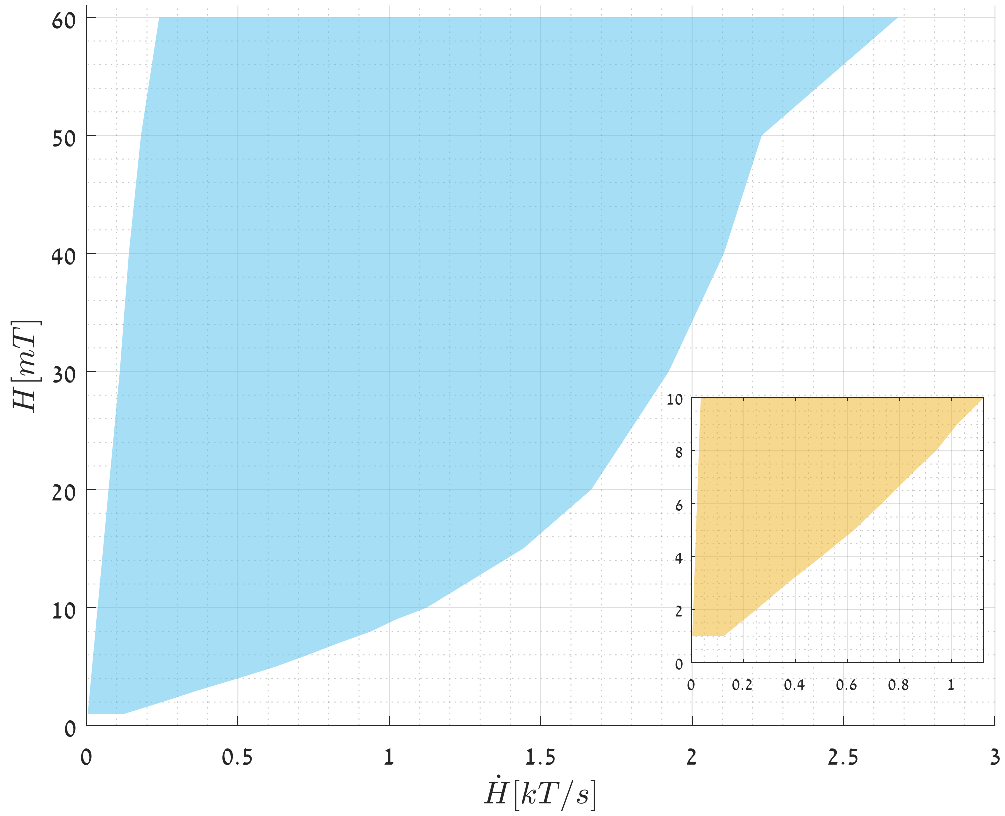

Figure 2.3.2: A diagram showing the possible values of the applied magnetic fields and ramping rates for the fast-switching system in the $H - \dot{H}$ plane, the range of the applied magnetic field H dependent on the applied ramping rate $\dot{H}$. The inset shows the possible ranges for low fields values in greater detail. The minimal possible ramping rate of $4.5\,T/s$ slightly increases with the applied magnetic field, while the maximal ramping rate increases more significantly with the applied field. The overall result is that measurements under small fields are much more restricted to a smaller range of slow ramping rates while high fields enable a wider range of faster ramping rates.

Another limitation, caused by both the fast nature of the dendrites nucleation and the fast-ramping rates of the magnetic field in our experiments, was on the detection of the higher threshold fields; The lower threshold field can be detected by finding the lowest field target to cause the nucleation and propagation of dendritic avalanches through the sample. However, the higher threshold field is defined as the highest field to cause dendritic avalanches. As our system increase the field rapidly and the camera cannot distinguish between sequential dendritic events, we could not accurately detect the higher threshold field[4]. For this reason, in this work we focused on the samples' lower threshold fields when considering high field ramping rates, and considered the

[4] For the detection of the lower threshold field, we change the maximal target field to which the magnetic field rise. The first target field to create an avalanche is the lower threshold field. this method does not allow the detection of the higher threshold field, because we cannot determine which dendrite was nucleated last, and at what field.

higher threshold field only for measurements done under slow ramping rates, when the distinguish between following dendritic events was possible and therefore the detection of the higher threshold field was possible as well.

In this work, we use the fast MOI system to observe dendritic avalanches under different ramping rates of magnetic field in our coated and uncoated samples. From these observations the dependency of the threshold fields on the ramping rate, as well as the effect of the ramp rate on the dendritic avalanches' morphology and general behavior in these samples, can be found.

2.4. SQUID magnetometry

In order to find the samples' critical current density and its dependency on the external field, SQUID (Superconducting Quantum Interference Device) magnetometry measurements were performed on a representative sample from the same fabricated batch as the rest of the measured samples. Using the measured hysteresis loops width, ΔM, the critical current density as function of the external field $j_C(H)$ can be calculated using the Bean model [42] and the Kim model [43]. A representative set of magnetization measurements at different temperatures is shown in figure 2.4.1a. The critical current, j_C, shown in figure 2.4.1b is derived as $j_c = 30\Delta M/w$, where the pre-factor considers the geometry of the square film, and w is the sample half-width.

(a) (b)

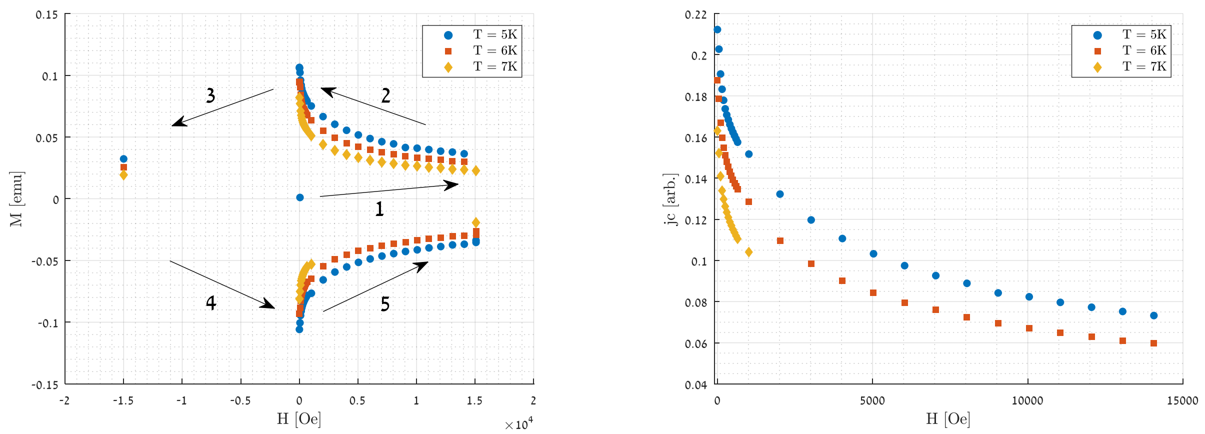

Figure 2.4.1: a) A representative set of hysteresis loops at different temperatures. b) The critical current density vs the external field H, derived from the data in figure 2.4.1a.

2.5. Data and MO images processing

Using simple image post-processing of frame subtraction and Fourier transform with the MATLAB software, we cleaned the raw MO images received from the experiments; First, a reference frame of the sample under zero magnetic field were subtracted from the final images exhibiting flux penetration, in order to reduce bias noises. Then, the MO images were Fourier transformed and filtered from periodic noises the indicator introduces due to interference of the laser's light. The effect of this filtering process can be seen in figure 2.5.1, from the comparison between the original MO image in (a) and the cleaned images in (b) and (c).

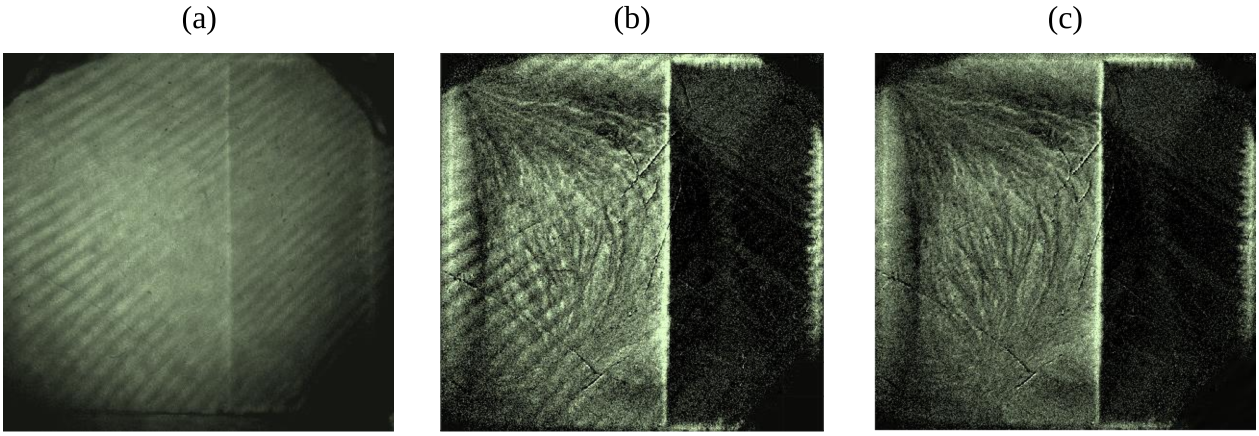

Figure 2.5.1: a) Original MO image as received from the experiment. b) processed MO image after subtraction of reference frame under zero field. c) Processed MO image after reference subtraction and periodic noise filtering.

In some cases of extremely poor contrast, particularly in measurements under slow ramping field where few following avalanches nucleated one after another, we subtracted following frames (in addition for the reference subtraction) to emphasize the last fast-occurring changes in the samples only. This way we can observe a clearer image of the dendritic avalanches without the contribution of the slow advancing flux in the image.

With further calibration process of the light intensities from the MO images, we can also translate the light intensity from the images into the local magnetic field in the sample. the calibration process is done by the following steps: 1) taking an image with the camera stutter closed, we measure a "dark image", D, of the electrical noise of the camera with no dependency on the light. 2) Next, image of the sample and indicator at zero external field is taken, for the light beam distribution, giving us the Zero-Field image (ZF). This image allows us the reduction of noise levels and normalization of the light intensity against its gaussian non-homogenous distribution. 3) The last images series, $calib(i)$, is of the indicator, far from the sample so that its magnetic behavior won't affect the results, and at increasing magnetic fields $H_Z(i)$. With those three measurements, we can build a calibration table of the field $F(i)$ against the magnetic field $H_Z(i)$:

$$(1) \quad F(i) = \frac{calib(i) - ZF}{Zf - D}$$

From this relation, the light intensity can then be translated back to magnetic field, giving us the local field across the sample.

2.6. COMSOL physical simulations

For further understanding and discussion of the results and observed phenomena, we use the COMSOL Multiphysics software, to simulate simple models of our samples and to compare the results with the experimental ones. The COMSOL software use finite element analysis and solving for various physical and engineering applications, such as coupled phenomena and Multiphysics. By facilitating conventional physics-based interfaces and coupled systems of partial differential equations, the COMSOL allow the modeling of the samples' physical behavior.

In this work, two different models were made and discussed. The first model, constructed by Itay Garofy, simulated the behavior of a partially superconductor-coated superconducting sample, by considering the superconductor as a simple strong diamagnetic material, both layers to be of the same parameters, and raising the external field around it. The second simulation, prepared by Yasha Nicolshin, used a more precise modeling of the sample, by considering the specific superconducting behavior of the sample.

3. Results

3.1. Metal coating

In this section we describe the effect of partially coating a NbN sample with a metallic Cu layer. We show the results for sample A at its different coating stages; A_I, A_{II} and A_{III} (these stages are described in the sample fabrication section 2.1).

Initial MOI measurements were performed on the bare NbN sample, A_I, in order to have a reference point to compare the later coated results to. Using our MOI system with slow ramping field of $2\ mT/s$, we found the sample's threshold temperature, T_{th}, below which the sample is thermomagnetic unstable and magnetic flux enters sample A_I as dendritic avalanches (either as positive or negative dendrites, as can be seen in figure 3.1.1 below); for positive dendritic avalanches we found it to be $T_{th}^{\uparrow} = 4.5\ K$, while for negative dendrites we found a threshold temperature of $T_{th}^{\downarrow} = 4.8\ K$. At higher temperatures sample A_I was stable, and the flux entered and exited the sample smoothly, according to Bean's profile.

Since at temperatures lower than T_{th} the sample is already unstable even at ramping rates low as $\sim 2\ mT/s$, detecting any significant dependency of the threshold fields on the ramping rate was impossible with our experimental setup. For this reason, we conducted the next measurements at temperatures above T_{th}, and under much faster ramping rates. That way a new unstable regime is opened by the high sweeping rate of the field, where we could find a more significant dependency of the instability threshold fields on the ramping rate.

It is also interesting to note here that the threshold temperature for anti-dendrites is higher than that of positive dendrites, and that we also observed that for a specific temperature, sample A_I suffer from anti-dendrites under a wider range of magnetic fields. This behavior repeats itself in other samples as well and can be explained by the different critical currents under increasing and decreasing fields due to the remnant magnetic field trapped in the sample (as can be seen in image 3.1.1b); The trapped flux during the field decrease reducing the sample's critical current, as was explained in the introduction section. From this result we can conclude the instability regime of anti-dendrites is larger than the instability regime of positive dendrites. However, though the anti-dendrites can offer a wider instability regime and are expected to show similar overall behavior as the positive dendrites, the threshold values of the anti-dendrites showed larger noise, and so we chose to focus in this work on the positive dendrites only and to mostly disregard the behavior of the anti-dendrites in the sample and the effect of the field ramping rate on them.

(a) (b)

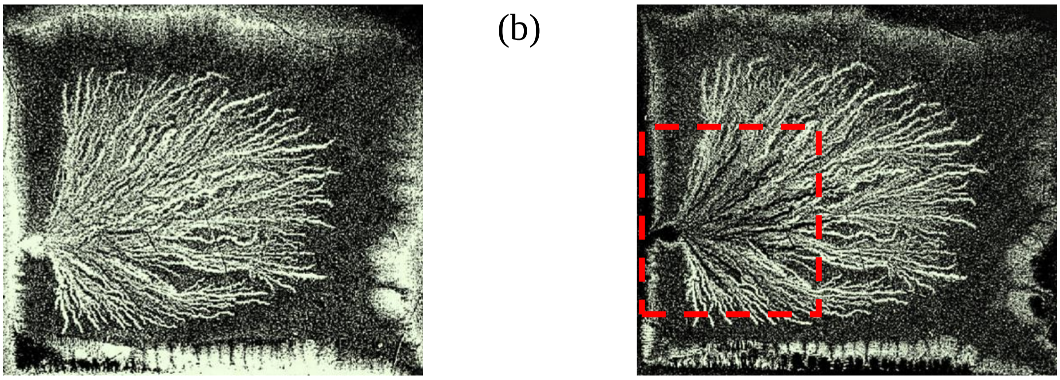

Figure 3.1.1: a) Positive dendritic flux avalanche, occurring at increasing magnetic field from 0 to 4 mT. b) Negative dendritic flux avalanche (anti-dendrite) on the previously existing positive dendrite's stem (in the red frame), occurring at decreasing magnetic field from 4 to 0 mT. Both images are of sample A_I, taken sequentially at temperature $T = 5.5\,K$ and ramping rate $\dot{B} = 0.04\,kT/s$ (the same rate for the field's ramping up and down). Negative dendrites exhibited a larger instability region than the positive dendrites but suffered greater noise levels.

Following MOI measurements of sample A_I in temperatures above $T_{th}^{\uparrow} = 4.5\,K$ and under higher ramping rates were performed next, using our unique MOI system. As we increased the sweeping rate, dendritic avalanches begun to nucleate and advance through the sample at higher, previously stable temperatures. Like in the instability regime below T_{th}, the avalanches still appeared only in the interval between some lower and upper threshold field values, $H_{th}^{1} < H < H_{th}^{2}$. However, Unlike at $T < T_{th}$, above T_{th} we could clearly see the dependency of both the avalanche dynamics and their threshold fields on the magnetic field rising rate, as can be seen in the representative MO images in figure 3.1.2 and from the threshold field results gathered in figure 3.1.3 below. From images a and b in figure 3.1.2 we can see that as the field's ramping rate increases, bigger and more branched dendritic avalanches are nucleated and advance further into the sample. This behavior is similar to the effect increasing the magnetic field has on the appearance of the dendritic avalanches; higher fields causing larger, more branched and deeper dendrites.

We can also observe from the images in figure 3.1.2. the dendrites have a clear preference to nucleate along the sample lower left edge, where a sharp slit is present[5]. This preference can be understood by considering the local higher field such an indent induces, as was explained in the introduction section before, making this slit the weakest point to resist the nucleation of avalanches and the first point of entry for the dendrites.

(a) (b) (c)

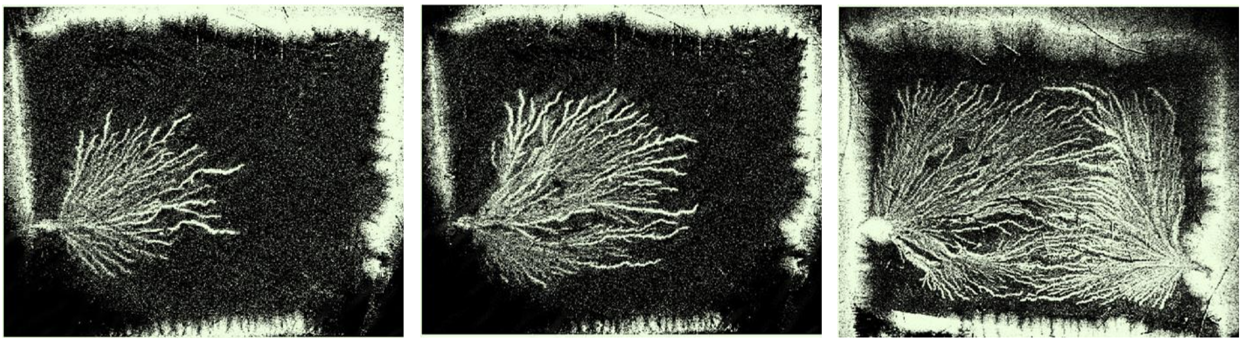

Figure 3.1.2: MO images of dendritic avalanches, occurring at temperature of $T = 7\ K$, magnetic field of $\mu_0 H = 2.2\ mT$ and field ramp rate of a) $\mu_0 \dot{H} = 0.12 \frac{kT}{s}$ and b) $\mu_0 \dot{H} = 0.15\ kT/s$. With increasing ramping rate, the avalanches are bigger and penetrate deeper into the sample. c) Another MO dendritic avalanches at $T = 5.5\ K$, $\mu_0 H = 5\ mT$ and ramp rate of $\mu_0 \dot{H} = 0.05\ kT/s$. At high enough ramping rates a few avalanches can penetrate from different nucleation spots along the edges.

However, as is seen in image 3.1.2c, under high enough fields and ramping rates, additional dendrites manage to enter the sample through other spots along sample A_I's perimeter as well. The contribution of the higher field and ramping rate to the magnetic pressure on the sample un-stabilizes other points along the sample perimeter and allow the nucleation of additional avalanches there.

Another thing we can observe from the images in figure 3.1.2 is the fact that although the branches of the avalanches tend to avoid one another and spread wide (like in images a and b), under enough magnetic stress some branches seem to collide with one another regardless, as can be seen in image c, and even form passages of trapped flux that cross the entire sample from one side to the other.

[5] This slit was caused by sample A_I's mechanical cutting and can be seen more clearly in figure 3.1.1 in the sample fabrication chapter.

By searching for the lowest field to cause a dendritic field for a specific field ramping rate, we found sample A_I's lower threshold field, the results for few different sample temperatures are gathered and shown in figure 3.1.3 below.

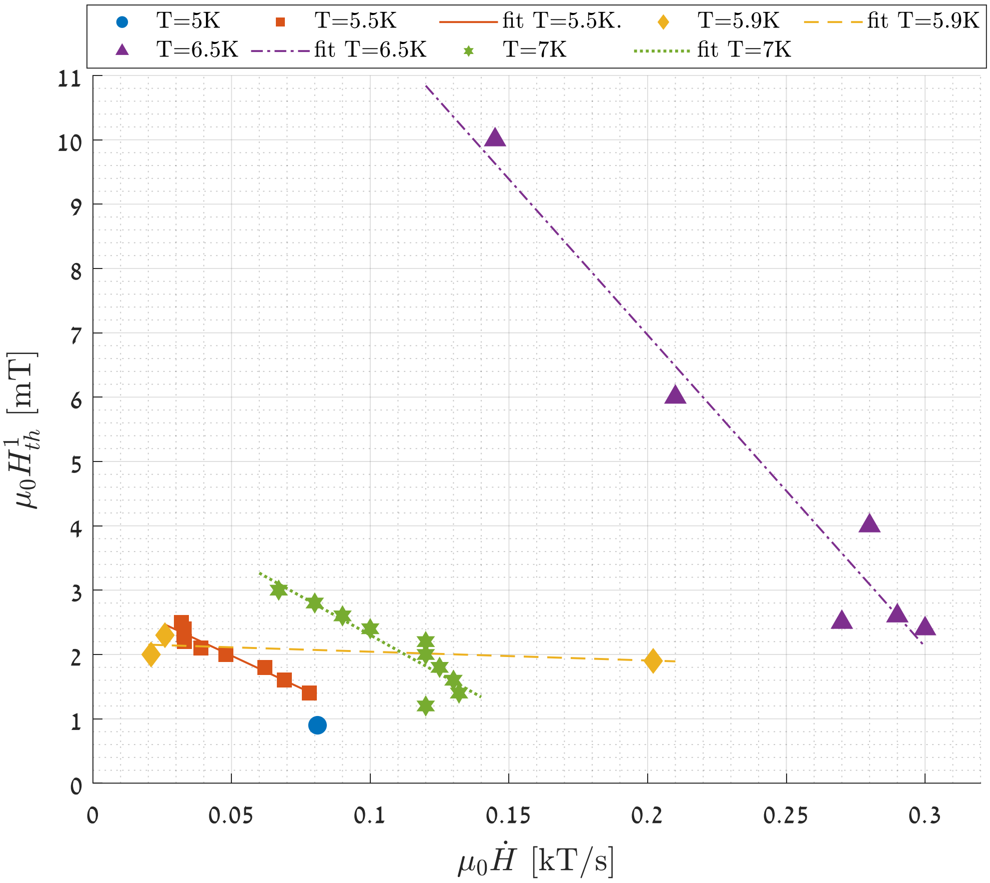

Figure 3.1.3: The lower threshold field, $\mu_0 H_{th}^1$, dependency on the magnetic field's rising rate, $\mu_0 \dot{H}$, for sample A_I at different temperatures. All the results shown here are for positive dendrites at increasing field.

As can be seen from the different curves in figure 3.1.3, sample A_I's lower threshold field, $\mu_0 H_{th}^1$, decreases with increasing ramping rate. Some of the measured temperatures, like $5K$ and $5.9K$ presented technical difficulties (as was described in detail in the experimental section above) and therefore suffer from lack of sufficient data points. However, considering the other curves plotted in figure 3.1.3 of $T = 5.5, 6.5, 7\ K$, we can see a clear behavior; the threshold field decreases, quite linearly, with increasing ramping rate of the magnetic field. Such behavior is consistent with previous works and theory, as was explained in the introduction. Higher ramping rates of the magnetic field induce higher electrical fields in the sample, and in turn generate greater heat through the movement of the vortices in the sample. Because of that, the sample is closer to becoming unstable and requires only a smaller added contribution from the external field to reach the threshold state for the nucleation of the first dendrite. As a result, the lower threshold field decreases as the field ramping rate increases.

When considering the effect of the temperature on the curves in figure 3.1.3, however, we can detect an unexpected behavior. From $5K$ and up to $6.5K$ we can see an overall rise of the $\mu_0 H_{th}^1(\mu_0 \dot{H})$ curve. However, the threshold field results at $7K$ show a deep decrease again. We would have guessed that with increasing temperature the threshold values will monotonically increase as well, since with higher temperature the sample becomes more stable (and in fact we had to use such high ramping rates to open an instability regime at those temperatures in the first place). For this reason, the strong decrease in the threshold values between $6.5K$ and $7K$ is problematic and can hint on some interfering influence.

One such possible influence can be small variations in the quality of the thermal contact between the sample and the cryostat's cold finger. Since the thermomagnetic instability is strongly dependent on the heat removal from the sample, small changes of the thermal contact during the sample mounting between measurements and throughout the measurement itself (due to small mechanical vibrations of the system and the repeating heating and cooling of the sample chamber under high vacuum) can lead to large differences in the measured threshold fields.

Next, in order to see the effect of metallic coating layer on the suppression of dendrites under fast ramping magnetic fields, sample A was partially coated with a 150 nm thick Cu coat layer (as was described in detail in the samples fabrication section). However, MO images of sample A_{II} did not show the coating layer having any significant effect; dendrites nucleated all along the samples edges and propagated through the sample with no clear differences between the coated and uncoated areas we could detect. Initial measurements of the threshold fields did not show any differences from A_I's results as well.

As was explained in the introduction section, previous works already tied the coat layer thickness to its suppression efficiency, S, due to the dependency of the induced eddy currents on the metal layer thickness; a thicker layer holding larger eddy currents [25]. We can therefore explain the coating layer having no clear effect due to it being too thin. In the discussion section, we will further analyze the thickness dependency of the avalanches' suppression in sample A_{II}.

Since sample A_{II} showed no sufficient avalanche suppression, we did not measure the dependency of its threshold fields against the field ramping rate, and instead continued and coated the sample by an additional 300 nm thick Cu layer, to increase its suppression efficiency S, as was described above.

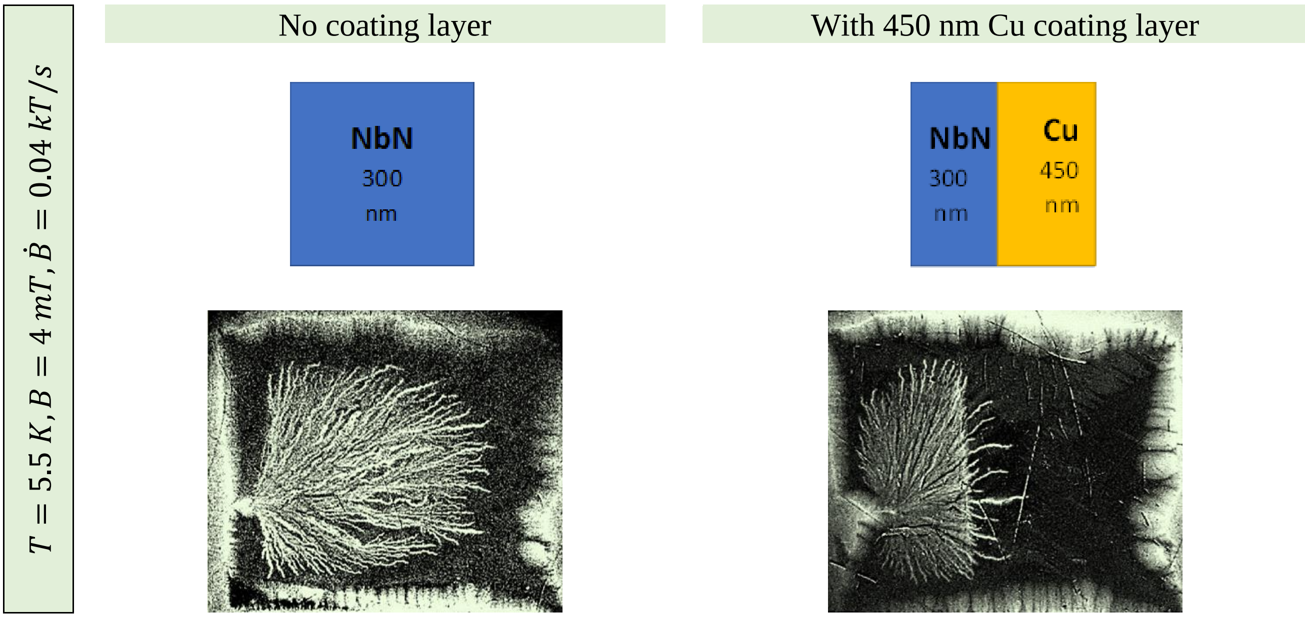

Figure 3.1.4: Comparison of dendritic avalanches in sample A_I and sample A_{III}. It can be easily seen that sample A_{III} offer a suppression of the flux avalanches under the coated area. Most of the advancing branches are stopped completely along the coat edge, with only a few that manage to cross it. Furthermore, even the branches that do manage to cross the boundary stop after only a small penetration depth.

Finally, the 450 nm Cu partially coated sample, A_{III}, shows a significantly different response to dendritic avalanches than the bare sample A_I, as can be seen in figure 3.1.4 above. From the MO image of sample A_{III}, we can see the dendritic avalanche nucleates in the uncoated area and propagate towards the Cu layer's boundary. Then, most of the dendrites' branches that reach the boundary between A_{III}'s uncoated and coated areas are stopped. A few of the branches do manage to penetrate the coated area, but they too stop after a much shorter entry depth in comparison for the dendritic avalanche's penetration depth in the bare sample, A_I. As such, we can observe a clear suppression of the dendrites by the metallic coating layer in sample A_{III}.

However, though the Cu coat shows a good suppression of the dendritic flux avalanches, it does not show any suppression of the smooth flux penetration from the sample edges. This difference can be understood by considering the difference in the advancing velocity of the magnetic flux; The smooth flux entry is much slower, and so the Cu layer do not induce strong eddy currents to resist its entry and does not affect it.

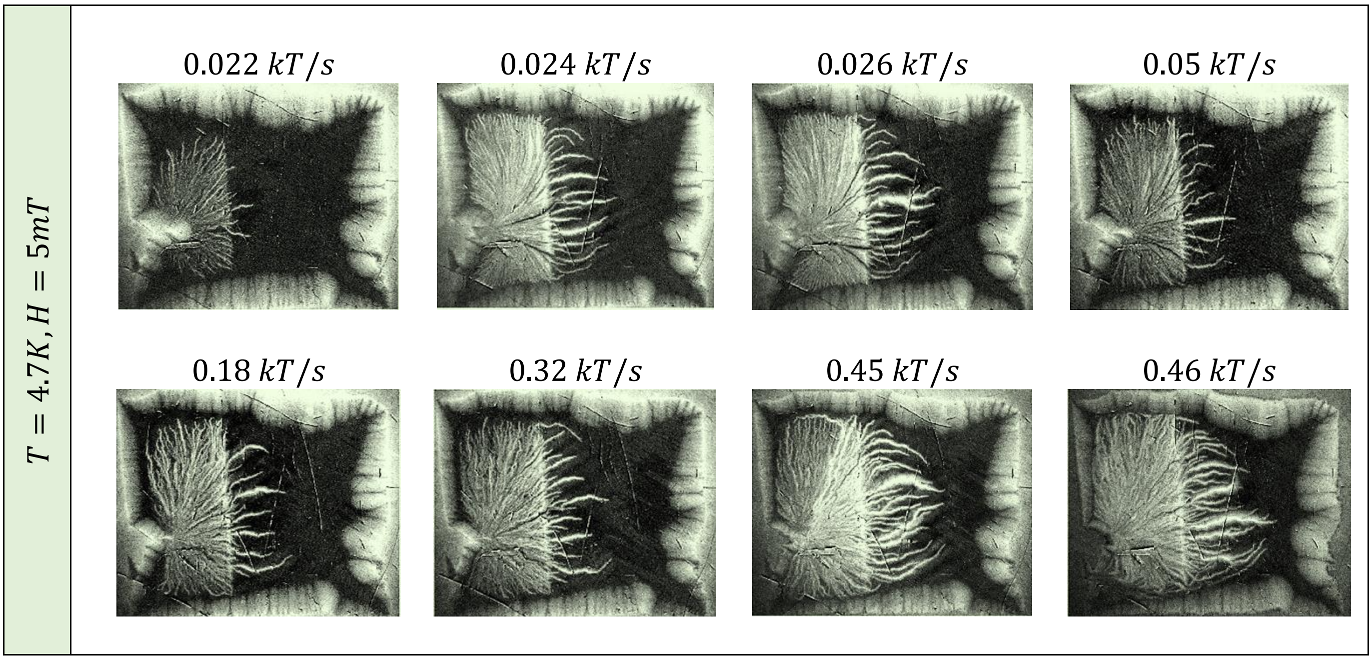

Figure 3.1.5: series of MO images of dendritic avalanches in sample A_{III} taken at different field ramping rates. All images were taken at $T = 4.7K$ and $H = 5\ mT$.

The response of the coated sample A_{III} to magnetic flux avalanches was then measured against varying ramping rates, some representative MO images are gathered in figure 3.1.5 above. A few observations can be made from those images: Most of the dendritic branches stop at the boundary between the uncoated and coated area or are even redirected back to the uncoated area. Still, at all the measured rates there are always a few branches that manage to cross the boundary, more branches crossing with increasing ramp rate. Additionally, the branches that do manage to cross also advance deeper into the coated area as the rate increase. Another observation to be made is the fact that dendrites that advance under the Cu coat layer seem to be wider compared to the thin branches seen in the uncoated area, and do not continue to branch further. And lastly, it is clear that the dendritic avalanches nucleate only along the uncoated edges of sample A_{III}, a fact that remained even at higher magnetic fields and faster ramping fields (not shown here). It is important to remind here that though dendrites preferred to nucleate at the indent along the lower left edge for samples A_I and A_{II} as well, under high enough fields and ramping rates, they suffered from dendrites' nucleation at different points along the sample edge too. A_{III}, on the other hand, did not suffer from any avalanche nucleation under the coated area for any field and ramping rate we measured with our experimental setup.

Plotting the number of dendrites that manage to cross the Cu coat boundary, as well as the maximal entry depth of those crossing branches into the coated area, we get the results presented in figure 3.1.6. below. Both the crossing branches' number and depth show a similar non-monotonic behavior; a sharp increase at the lower rates, followed by a sharp decrease at moderate rates (around $\sim 0.1\ kT/s$), and a slower but overall higher increase at higher rates.

We can explain these results by considering the different and opposite effect of the field ramping rate on the magnetic flux avalanches and on the eddy currents in the Cu coat layer, each effect overcoming the other at a different range of ramping rates.

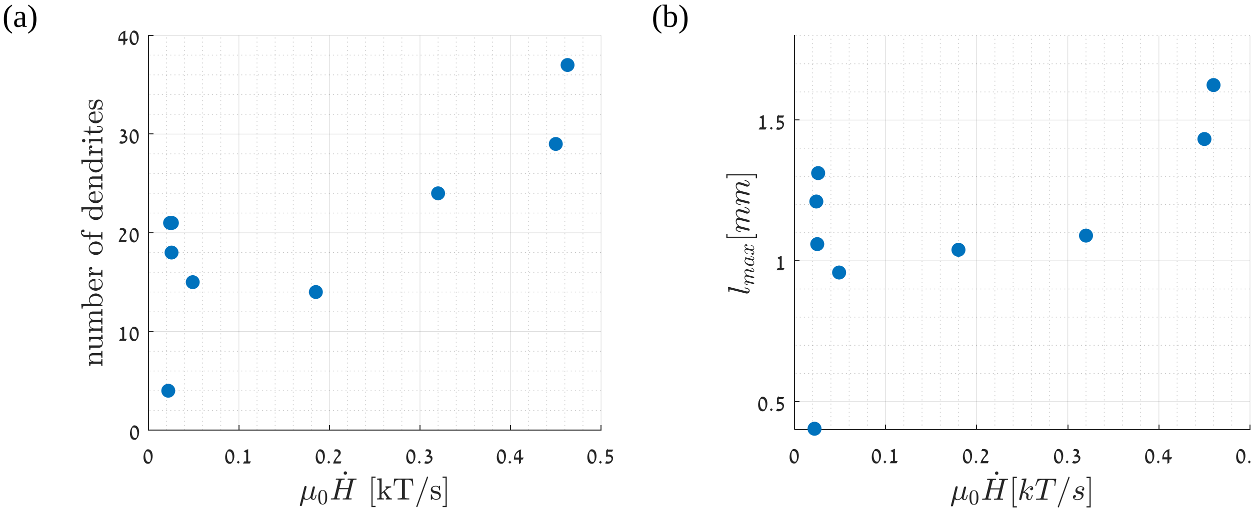

Figure 3.1.6: a) number of dendritic avalanches' branches crossing the Cu-coat boundary with increasing field ramping rate. b) maximal penetration depth of the crossing dendrites into the Cu-coated area with increasing ramp rates.

Lastly, we searched again for the lowest field value at a given ramping rate to cause an avalanche, thus finding sample A_{III}'s threshold field dependency on the ramping rate. The curves for few different temperatures are shown in figure 3.1.7. below. We can see that like the results for A_I, the threshold field curves for A_{III} in figure 3.1.7. decrease with increasing rate. However, here the dependency is not linear, as we see a sharper decline in the slower ramping rates ($\sim 0.2\ kT/s$) than in the higher rates, where the curves near a linear decrease again. Both the curves for $5\ K$ and $5.5\ K$ show a very close result (due to experimental limitations, the curve for $4.7\ K$ suffered from a lack of data points), quite unlike the case for the bare sample where we saw much more significant variations of the curves with temperature. This behavior can be understood by considering the metallic Cu layer acting as a heat sink and another heat outlet for the sample, thus thermally stabilizing it and reducing the effect of thermal coupling variations between the sample and the cryostat's cold finger.

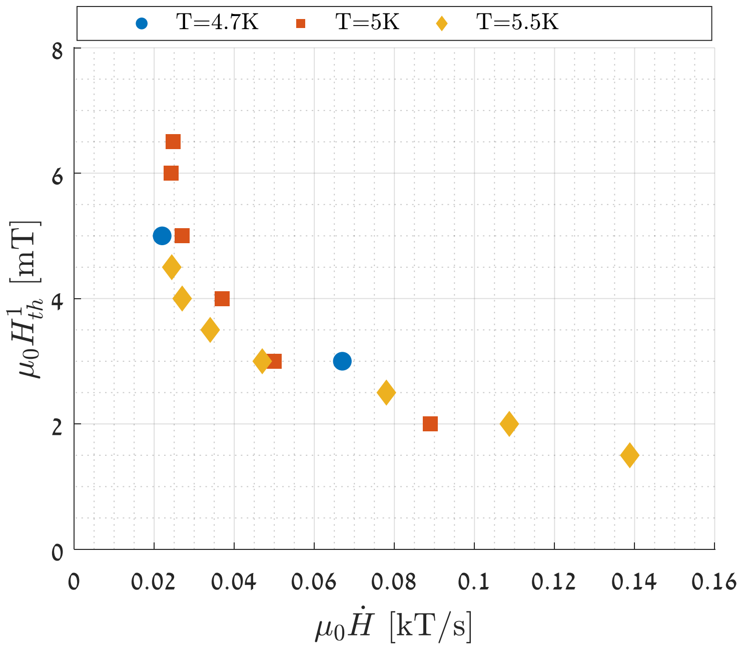

Figure 3.1.7: The lower threshold field, $\mu_0 H^1_{th}$, dependency on the magnetic field's rising rate, $\mu_0 \dot{H}$, for the coated sample A_{III} at different temperatures. Here we can see the threshold fields decreases with increasing ramping rates, with a sharper decrease at the lower ramping rates.

Another important point to make is that due to the fact all the avalanches we observed in sample A_{III} nucleated in the sample's uncoated area, and some of the dendritic branches managed to cross the boundary, the threshold fields plotted here are for avalanches of the entire sample; meaning that even partial coating of the sample increase the stability of the entire sample. This result is quite surprising, as we did not expect the coating layer to affect the sample and help suppressing dendrites even outside of its area.

The comparison of the threshold fields of the bare sample A_I and the coated sample A_{III}, as well as a deeper analysis of the Cu layer contribution to the suppression of the dendritic flux avalanches will be held in the discussion chapter.

3.2. Superconducting coating

In this section we describe the effect of partial coating of a NbN layer with an additional superconducting layer of Nb. We show the results of two samples; sample B, with Nb coating thickness of 300 nm and sample C, with Nb coating thickness of 450 nm (as is shown in the schematics in figure 3.2.1 below and as was described in detail in the sample fabrication chapter).

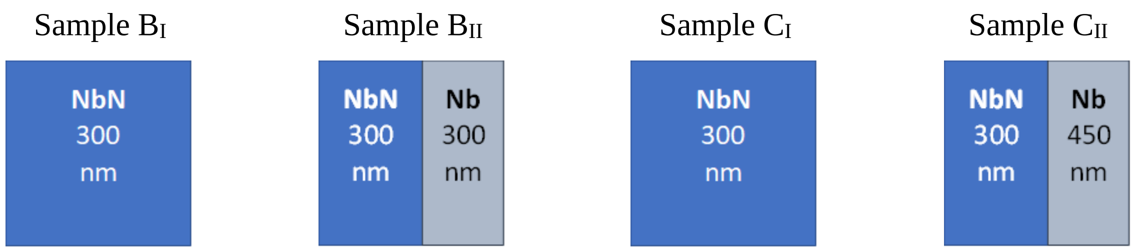

Figure 3.2.1: schematics of bare samples B_I and C_I and the partially coated samples B_{II} and C_{II}.

Initial MOI measurements were performed on the bare NbN samples, B_I and C_I before their coating with the additional Nb coating layer (with sample C_I acting as a representative sample of the batch). Under slow magnetic field ramping rate of $\dot{B} = 2\, mT/s$, we found the threshold temperature for positive dendritic avalanches to be $T_{th}^{\uparrow} = 4.6\, K$, a close result to the threshold temperature we found for sample A_I in the previous section: $4.5\, K$[6].

Like in the case for sample A_I, at this slow ramping rate of $2\, mT/s$, sample C_I suffered from dendritic flux avalanches only at temperatures below its threshold temperature. And as we mentioned previously in the Cu-coating section, at such slow ramping rates our experimental setup is limited and cannot be used to determine any significant dependency of the threshold fields on the ramping rate of the magnetic field. Therefore, in order to study the effect of the field ramping rate on the behavior of the dendritic avalanches, the following measurements were again performed

[6] The similar threshold temperatures of samples A_I, B_I and C_I are a good indication for the bare samples having similar initial instabilities regimes despite their varying sizes. Usually, larger sized samples suffer more severe instabilities, since the thermo-magnetic instability is strongly size dependent. In our case, sample A is a small sample ($4.5 \times 3.8\, mm^2$), but, as it suffers many indents along its edges that helps the nucleation of avalanches, we matched its overall instability regime to the instability of the bigger, yet smooth-edged, samples B and C ($5.5 \times 5.5\, mm^2$). This match allows the later comparison of each coating method.

at higher temperatures and with higher field ramping rate, in order to open a new instability regime where the threshold fields are much more dependent on the field ramping rate.

MO images of the dendritic avalanches above T_{th} and under fast ramping fields in sample C_I show the same behavior that was observed in sample A_I; The dendritic avalanches nucleate at the sample edge and advance towards the sample's center. As the ramping rate increase, more dendrites nucleate at the sample's edges, the nucleated dendrites bigger and advance further into sample C_I as well. We also repeated the measurement of the lower thresholds fields required to introduce avalanches to sample C_I against different field ramping rates and at different temperatures, the results gathered in figure 3.2.2 below. Unlike in the case of sample A, here we received a less consistent behavior at different temperatures.

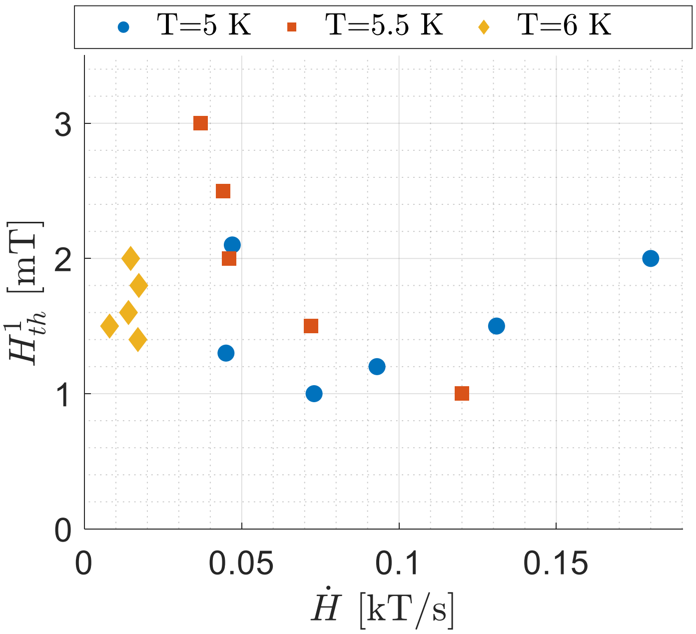

Figure 3.2.2: The dependency of the bare sample, C_I's, lower threshold field, $\mu_0 H_{th}^1$, on the magnetic field's rising rate for different sample temperatures. All the results shown here are for positive dendrites at increasing field.

From the $5K$ curve in figure 3.2.2 we can see a non-monotonic behavior, where the threshold field first decreases and then increases with increasing ramp rate. This result contradicts both the theoretical explanation and our previous experimental data, and therefore should be taken with suspicion, as it might be largely influenced by fluctuations in thermal coupling of the sample to the cryostat's cold finger, like we previously explained for the results of sample A_I as well.

At 5.5 K, on the other hand, we can see a behavior closer to previous measurements, where we see a monotonic decrease of the threshold fields with increasing ramping rates. As we previously explained for sample A_I, such behavior is expected and understandable; with increasing ramping rates, larger electrical fields are induced inside the sample, and as a result the heat generated by the moving flux is larger, and so the sample becomes much more unstable, leading to the decrease in the threshold field required to induce the first avalanche. Lastly, at 6 K we were near the system limit of measurements, and therefore could not find the dependency at higher rates, and so there is not a clear behavior we can learn from it.

Although we see here a noisy and unstable behavior with temperature, we considered the 5.5 K curve as the best indicator for the behavior of samples C_I and B_I, and proceeded with the coating of the samples, in order to study and compare their results for the metal-coated sample A.

Flux entry (either stable or unstable) in hybrid, partially superconductor-coated superconducting samples such as samples C_{II} and B_{II}, have not been studied much. For that reason, we'll dedicate few sections to consider the stable magnetic flux entry to such samples and the unstable flux entry of dendritic avalanches entry in slow ramping rates before continuing to present the results for fast ramping fields.

We first studied the stable flux entry above T_{th} into samples B_{II} and C_{II}, with slow ramping rate below 2 mT/s. Under those conditions the flux enters the samples smoothly according to Bean model. However, as can be seen from the MO image taken in $4.7K$ in figure 3.2.3 below, there is a clear difference in the flux entry profile between the uncoated and coated areas of sample C_{II}; The flux entry into the Nb-coated area being much shallower than the entry depth into the uncoated area. When further studying the different flux penetrations at different temperatures, MO images, like the ones presented in figure 3.2.3, showed that with increasing temperature the difference between the areas decrease and the coated area showed a closer flux penetration to the uncoated area. Finally, at temperature of $8.9K$, the difference closed completely, and the smooth flux penetration was homogenic across the sample, as can be seen from 8.9 K image in figure 3.2.3 below.

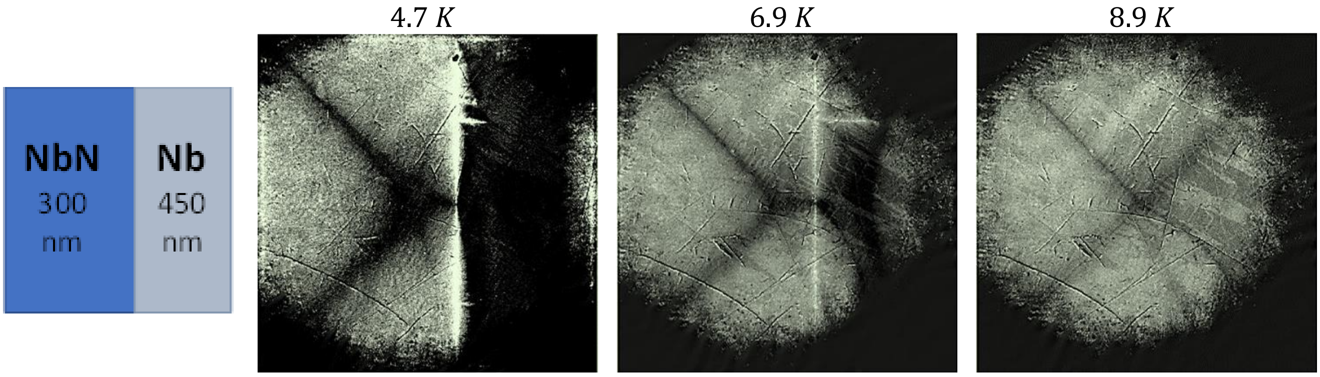

Figure 3.2.3: Schematic of the coated sample C_{II}, and a series of MO images in increasing temperatures of the smooth flux penetration into the sample. All images were taken at field $\mu_0 H = 1\ mT$ and after a slow field ramp of $\mu_0 \dot{H} = 2\ mT/s$[7].

This result repeated itself for sample B_{II} as well, and can be understood by considering the additional shielding the Nb coat layer provides to the underlayer NbN as a superconducting layer with its own Meissner currents. Additionally, since the Nb coat layer is closer to its critical temperature than the NbN layer[8], it is much more sensitive to changes in temperature in the temperature range we measured of $4.7 - 8.9\ K$; As the temperature increase the Nb layer shielding against smooth flux entry weakens, until at $\sim 9K$ It goes out of its superconducting phase completely, and no longer resist the entry of slow advancing flux whatsoever. Resulting in the homogenous flux penetration, like the one we see in the 8.9 K image in figure 3.2.3.

It is important to note that this behavior is very different to that observed for the case of metal-coating; In sample A_{III}, we did not detect any difference in the smooth and stable field penetration between the uncoated and coated areas, since the metallic layer does not resist the slow entry of the smooth flux penetration. The two cases come together, however, above $9K$, as the Nb coat layer becomes metallic and transparent to smooth flux entry as well.

By measuring the penetration depth of the flux entry fronts from MO images such as the ones in figure 3.2.3, we found the temperature dependency of the penetration depths into the coated and uncoated area, as well as the penetration depth difference, Δl^*, in sample C_{II}; The difference was calculated by subtracting the flux penetration depth into the right Nb-coated NbN edge, $l^*_{Nb-coated}$, from the penetration depth into the left uncoated NbN edge, $l^*_{uncoated}$. The results are gathered in figure 3.2.4 below.

[7] The round shape seen in the MO images here is due to the system's circular light beam, leaving the corners of the rectangular sample unlit.
[8] $T_C^{Nb} = 9K,\ T_C^{NbN} = 13.8K$.

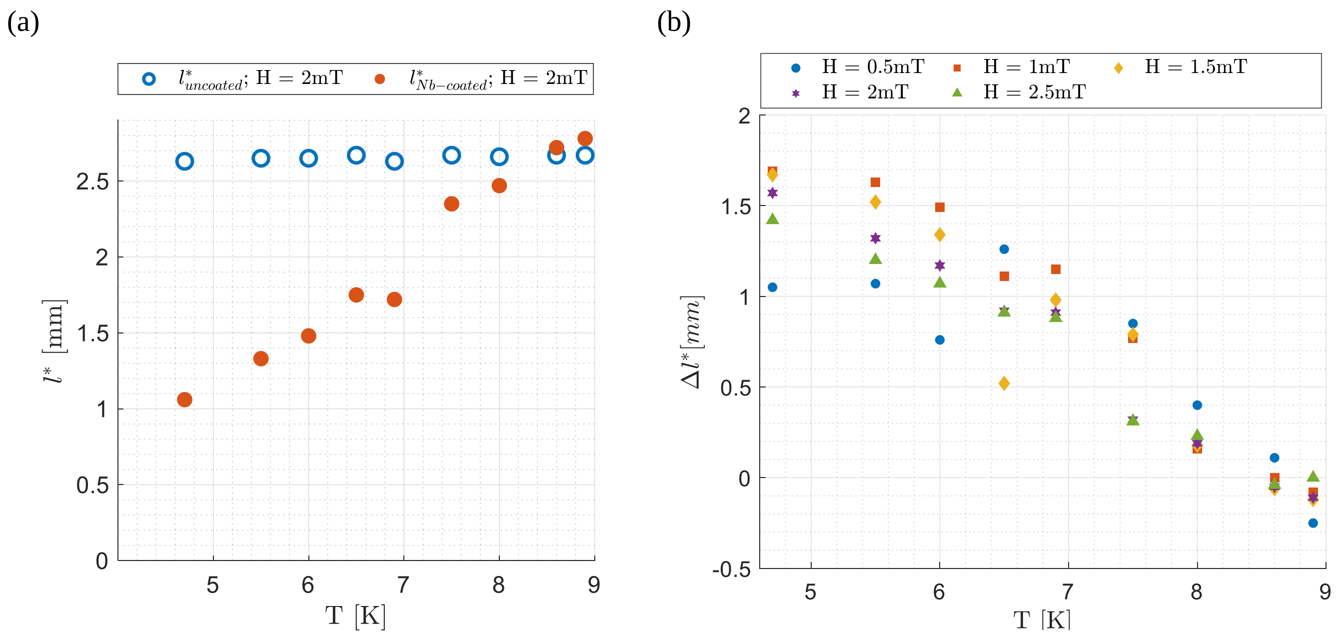

Figure 3.2.4: a) representative flux penetration depths into the left uncoated and right coated edges vs temperature in sample C_{II} and at external field of 2 mT. b) Difference in flux penetration depth, $\Delta l^* = l^*_{uncoated} - l^*_{Nb-coated}$, between the left uncoated edge and the right coated edge of sample C_{II} vs temperature and at different external magnetic fields.

As can be seen from the results in figure 3.2.4a, the Nb-coated area is much more sensitive to temperature than the uncoated NbN area, even at the lowest measured temperature of $4.7K$. The penetration depth into the Nb-coated area increases significantly with increasing temperature while the penetration depth into the uncoated area remains quite constant. Figure 3.2.4b further reveals the differences show a gradual decrease with increasing temperature; the decrease is sharper closer to the Nb layer's critical temperature and vanishes upon reaching it at $9K$. This gradual decrease is similar to the typical decrease the critical current density shows with increasing temperature near a superconductor's critical temperature, T_C. Since in type-II thin films the Meissner shielding currents reach the critical current density at the sample's edges, the shielding of a superconducting film decreases with temperature similarly as well. In the case of sample C_{II}, with increasing temperature the Nb layer near its phase transition, its critical current density decreases, and it becomes more 'transparent' for slow flux entry, until becoming metallic and completely transparent at its critical temperature. By also considering the curves of the different fields in 3.2.4b, we can see that as the external field is increased the flux penetration differences increase as well, but the overall dependency on the temperature is kept.

Next, considering the unstable behavior of samples B_{II} and C_{II} below T_{th}, and looking at dendritic avalanches formed in those samples at slow ramping rate of $2\ mT/s$, we observed some interesting and unexpected behaviors we will expand upon here. Some representative MO images of both samples at different fields and at temperature of $4.7K$ are shown in figure 3.2.5 below.

The first observation from the images in figure 3.2.5 is that dendrites nucleated along both the uncoated edges and the Nb-coated edges of both samples B_{II} and C_{II} (unlike the case in the Cu-coated A_{III}, where dendrites did not nucleate in the coated area). In sample B_{II} specifically, the dendrites had no preference for the first area to nucleate from, alternating between the coated and the uncoated area, and in many cases entered both simultaneously (such case is shown in the $3.2\ mT$ image of B_{II} in figure 3.2.5). sample C_{II}, on the other hand, first suffered from dendrites penetrating the uncoated NbN area (like the dendrite in the $3.2\ mT$ image of C_{II}), and only suffered dendrites entering the Nb-coated area at higher fields (like in the $6.4\ mT$ image of C_{II}).

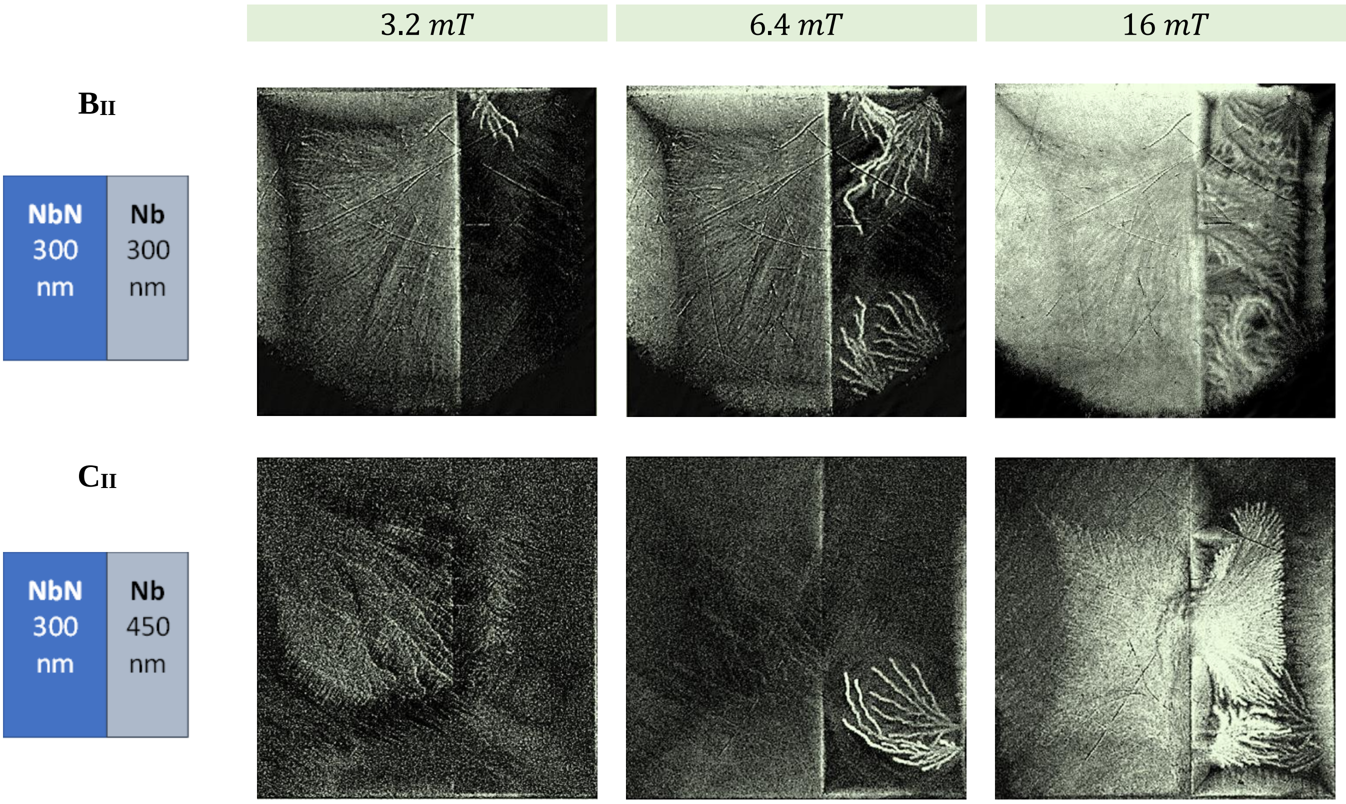

Figure 3.2.5: representative MO images of dendritic avalanches in samples C_{II} and B_{II} with increasing magnetic field. all images were taken sequentially below T_{th}, at $4.7K$, and at low ramping rate of $2\ mT/s$.

The MO images in figure 3.2.5 also show the inner coat layer edge strongly affects the dendrites that reach it from the uncoated area; stopping them sharply and completely up to some threshold value, dendrites managing to cross the coat layer edge into the coated area only above it (as is seen clearly in the 16 mT image for C_{II}, and with worse quality in the image for sample B_{II}).

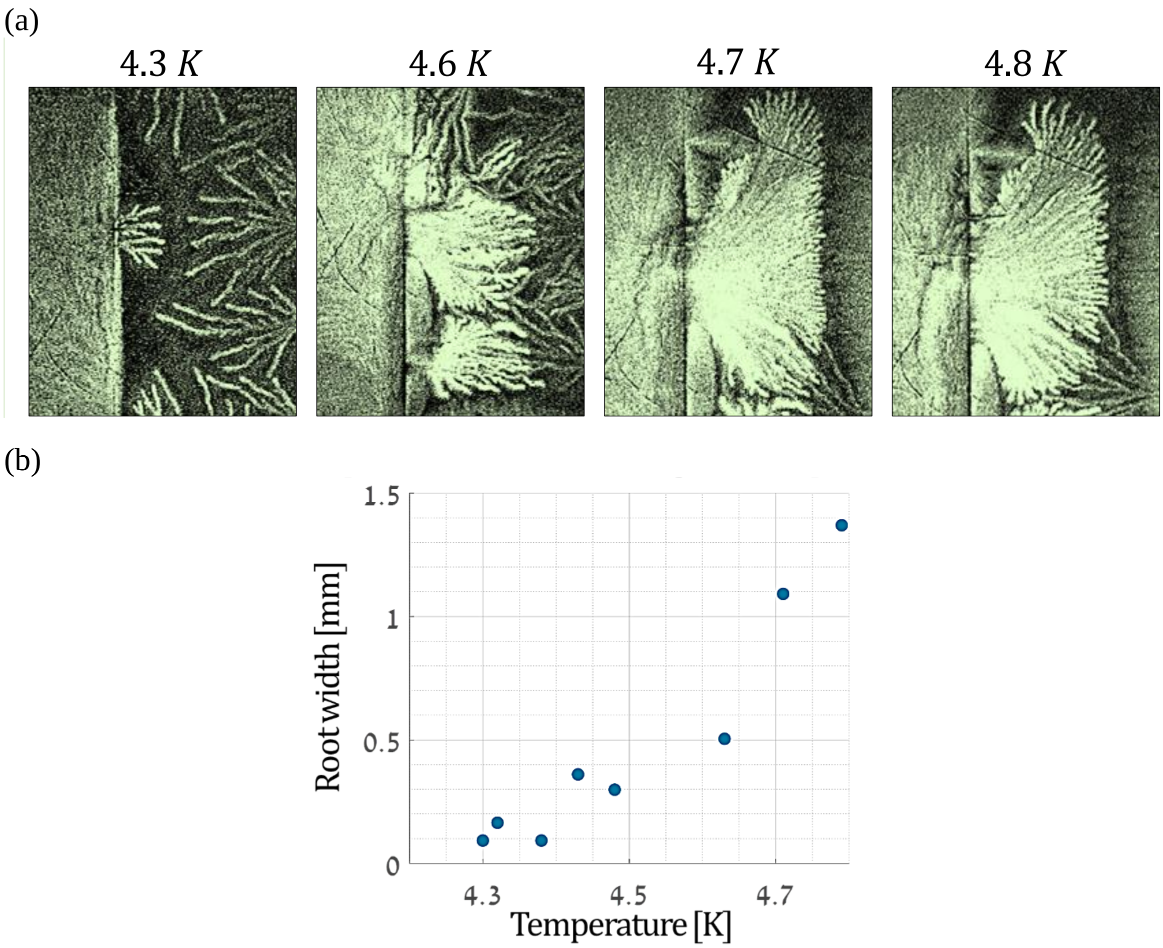

Figure 3.2.6: a) Enlarged MO images of the coat-boundary dendrites in sample C_{II} at different temperatures. b) Coat boundary dendrites' maximal root width vs temperature in sample C_{II}. the results were taken under slow ramping rate of 2 mT/s.

When further considering the dendrites that enter the coated area through the inner edge of the Nb coat (as can be seen in the 16 mT images in figure 3.2.5, and in figure 3.2.6a above), they do not simply continue existing dendritic branches that reach the inner coat boundary. Rather, they seem to be new dendrites that nucleate along the inner edge; they have a "root" of their own through which they enter the coated area, they penetrate the coated area perpendicularly to the coat edge, independently of the angle in which the dendritic branches from the uncoated area reach the inner coat edge, with branching that is mostly contained close to the nucleation "root". In most cases, the nucleation of the dendrites along the inner edge is also accompanied by the creation of anti-dendrites in the uncoated area and by the separation of the flux in the uncoated and the coated areas (the dark branches opposite to the dendrites in the coated area, and the dark boundary along the coat edge that can be seen in the MO images in figure 3.2.6a).

When also comparing the dendrites that nucleate along the inner coat edge at different temperatures, as is done in figure 3.2.6 above, a clear behavior can be observed; with increasing temperature, the nucleated dendrites enter through a wider root, with denser branches that fan out to a larger degree. The monotonic widening of the dendrites' root with temperature is presented in figure 3.2.6b. This behavior was previously observed and reported in regular thin superconducting films([10], [44], [45]), and further strengthen our claim for dendritic nucleation along the inner edge. In the discussion chapter, we will delve deeper into the possible cause for this observation and its meaning for the identification of new types of dendrites.

Another interesting observation to note is that, in both samples B_{II} and C_{II}, the shape of the dendrites that enter through the outer edges differs between the different areas of the sample; the dendrites that enter the uncoated NbN area have many long and thin branches, while the dendrites that enter the Nb-coated area are thicker, shorter, with less and slightly smoother branches. Those dendrites however, unlike the dendrites that nucleate along the inner edge of the Nb coat layer, do not show dependency on temperature in the range we measured. At a yet closer observation, such as the enlarged images in figure 3.2.7 below allow, we can see a slight difference in the shape of the dendrites in the coated area between samples B_{II} (in 3.2.7b) and C_{II} (in 3.2.7c) as well; the shape of the dendrites in the 300 nm Nb coated area of sample B_{II} looking closer to the shape of the uncoated NbN dendrites than the shape of dendrites in the 450 nm Nb coated area of sample C_{II}.

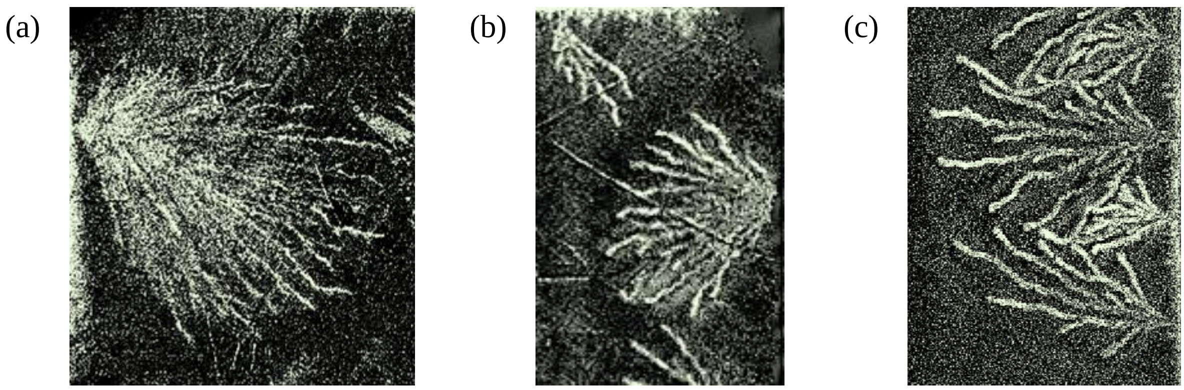

Figure 3.2.7: enlarged MO images of typical dendrites in a) bare and uncoated NbN, b) 300 nm Nb-coated area in sample B_{II}, and c) 450 nm Nb-coated area in sample C_{II}.

This difference in shape between the sample areas can also be clearly observed through dendrites that advance from the coated area into the uncoated area in sample B_{II}, as is seen in figure 3.2.8 below. From images 3.2.8b and 3.2.8c, we can see how the dendrites' branches change their form abruptly when crossing the boundary from the coated area into the uncoated area. It should be noted, however, that in this direction (from the coated area into the uncoated area) the dendrites do not show the nucleation-like behavior the dendrites show on the opposite direction. In the discussion chapter ahead, we'll explain further the cause for the different shaped dendrites we've seen here and use it to conclude the existence of new types of dendrites in our hybrid samples.

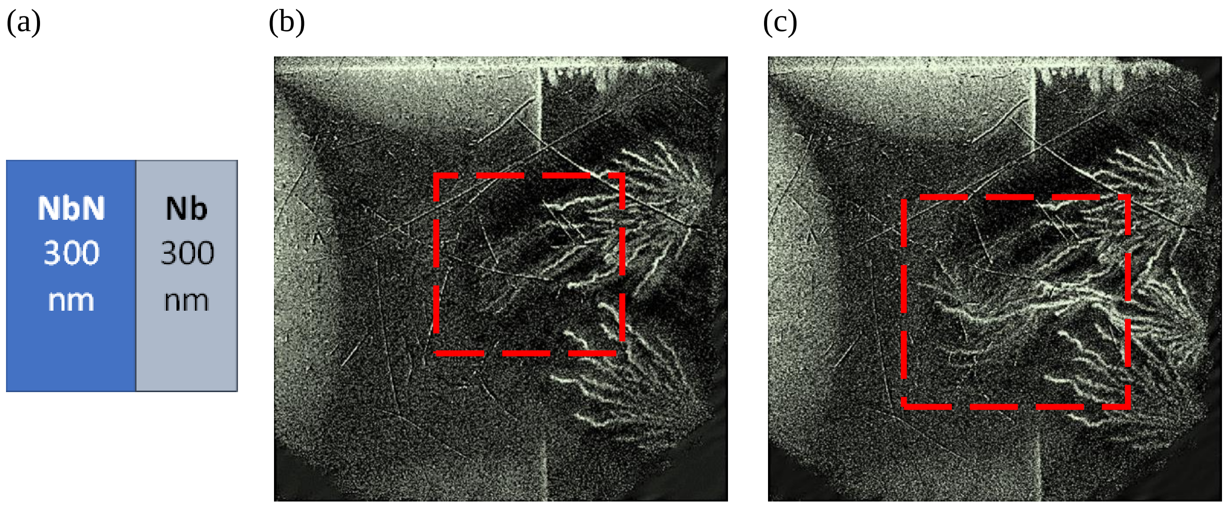

Figure 3.2.8: a) schematic of sample B_{II}. b,c) MO image of dendrites advancing from the coated area into the uncoated area at b) $\mu_0 H = 4\ mT$. c) $\mu_0 H = 4.9\ mT$. The red frames surround the crossing of the dendrites between the areas. Both b) and c) were taken at $T = 4.2K$ and $\mu_0 \dot{H} = 2\ mT/s$.

Next, we measured the whole unstable regime and found the upper and lower threshold fields' dependency on temperature[9]. Here, because of the clear separation of the dendrites in the samples' different areas, we make the distinction between the threshold fields of the uncoated area and the threshold fields of the coated area. The results of both sample B_{II} and C_{II} are organized in figure 3.2.9 below.

[9] Due to the slow ramping rates we used during this measurement, we could distinguish between avalanche events, thus finding even the upper threshold field above which no further avalanches occurred.

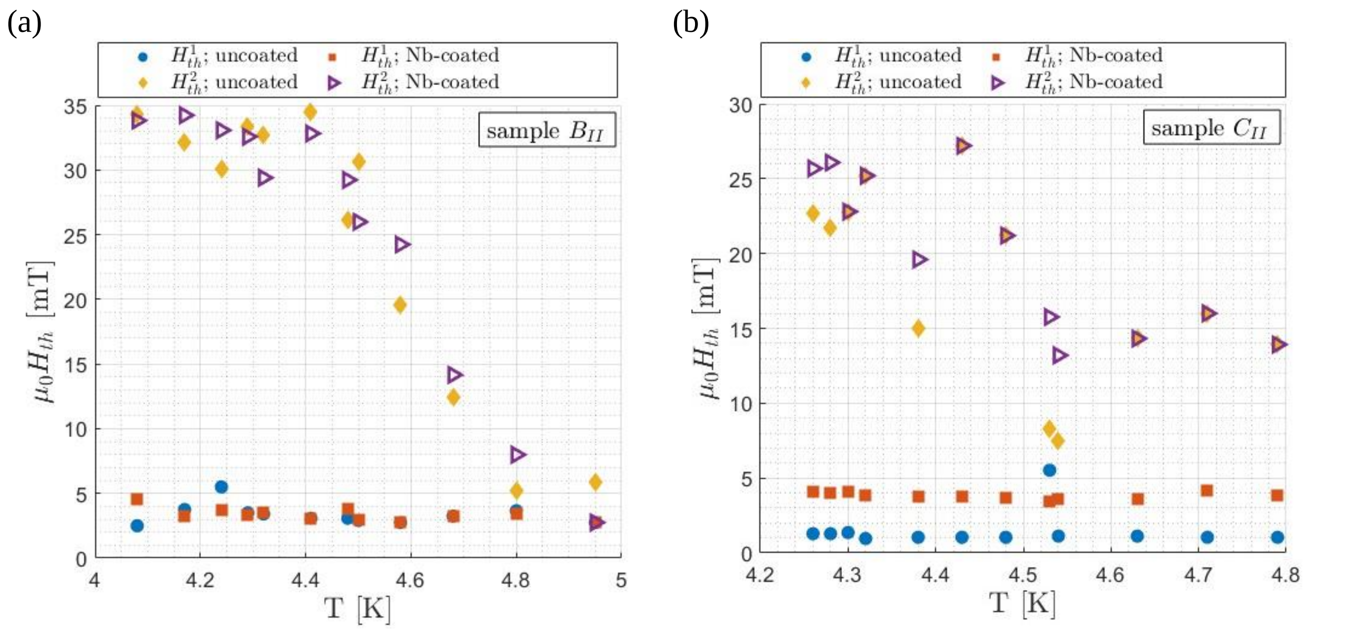

Figure 3.2.9: Threshold fields' dependency on temperature for slow ramping rate of 2 mT/s. The threshold values of the coated and uncoated areas were taken separately. a) Results for sample B_{II}. b) Results for sample C_{II}. sample C_{II} did not suffer dendritic avalanches above $4.8K$.

As we can see from the threshold fields of sample B_{II} in 3.2.9a, both the coated and uncoated areas show a classic dependency on the temperature; the upper threshold of both areas strongly decrease with increasing temperature, while the lower threshold field remains almost constant. The threshold fields finally meet at the threshold temperature $4.95\,K$, above which no dendritic avalanches nucleate at such low ramping rate. It is interesting to note that sample B_{II} do not show clear difference in the stability of the coated and uncoated unstable regimes, a quite surprising result, since we would have expected a more significant effect of an additional 300 nm thick superconducting layer. Based only on these threshold fields results we could have concluded that the 300 nm Nb coat layer had no effect on the thermomagnetic instability at all. However, as we saw above from the MO images of sample B_{II}, the Nb coat does affect both the stable flux entry and the shape of the dendritic avalanches. In the discussion chapter, we'll try to explain these seemly opposite results.

Sample C_{II} on the other hand, show a much more significant difference between the unstable regimes of the coated and uncoated areas, as can be seen in figure 3.2.5b. The upper threshold fields of both areas still decrease with increasing temperature but show noisier results than the upper thresholds in sample B_{II}. This noise is due to avalanches that manage to cross the coat edge boundary and penetrate both the coated and uncoated area in sample C_{II}, making the comparison

between the upper threshold fields difficult, though the threshold field of the coated area appears to be overall higher than the threshold field of the uncoated area.
The lower threshold fields, however, show much clearer results; the lower threshold field of the uncoated area is significantly lower than the threshold field of the coated area. Meaning that here, the coat layer does offer a suppression of the magnetic instability as we expected. This suppression could also be seen in the MO images of sample C_{II} in figure 3.2.5, as the first dendrites there always penetrated the uncoated area, and only penetrated the coated area at higher fields.

Lastly, another important result to consider is the threshold temperature of the samples. As we mentioned in the beginning of this chapter, the threshold temperature at ramping rate of $2\ mT/s$ for samples B_I and C_I, before the Nb coating stage, was around $4.6K$. From the instabilities diagrams in figure 3.2.9, however, we see the new threshold temperature at $2\ mT/s$ of both B_{II} and C_{II} is around $4.9K$; instead of stabilizing the samples, the coating seems to harm the samples thermomagnetic stability even further. Since the reason we studied dendritic avalanches in superconductor-coated samples in the first place was to study its avalanches' suppression, this result is very surprising and putting into question the very ability of superconducting coat layer to suppress dendritic avalanches. We will continue this essential discussion in the discussion chapter.

Next, after studying the stable and unstable flux entry into samples B_{II} and C_{II} at slow ramping fields, we continue to study the unstable flux entry at fast ramping fields. Since sample B_{II} did not show a clear difference between the coated and uncoated threshold fields, we continued to measure only sample C_{II}. And as in previous measurements under fast ramping rates, we conducted this part only above the sample's threshold temperature, in order to open a new instability regime, where the threshold fields are strongly dependent on the ramping rate.

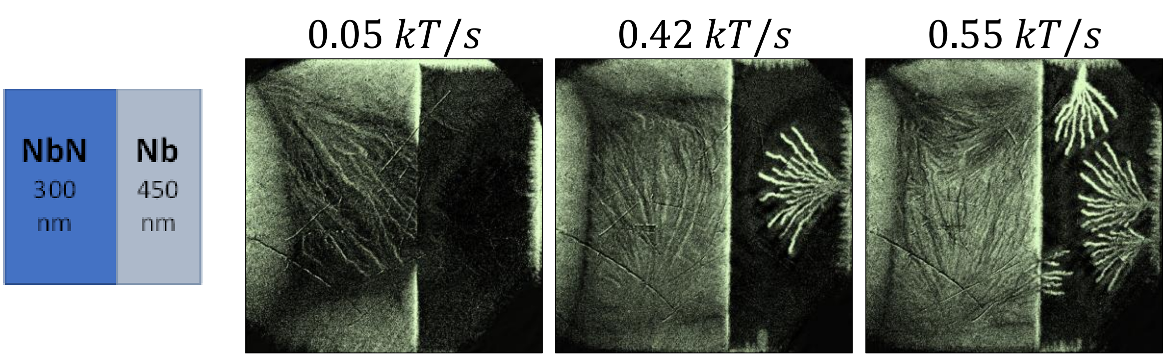

Figure 3.2.10: Effect of the field ramping rate on the dendrites in sample C_{II}, all images were taken at $T = 5.2\ K$ and $\mu_0 H = 5\ mT$.

Typical dendritic avalanches at increasing ramping rate are shown in figure 3.2.10 above. As can be seen from the MO images gathered there, the behavior of the dendritic avalanches with increasing ramping rates is very similar to their behavior with increasing fields we saw for slow ramping rate: At low enough ramping rates the dendrites enter only through the uncoated area and propagate there. Branches that reach the coat boundary are stopped abruptly and completely, and no dendritic branches enter the coated area whatsoever. As the ramping rate increase above some second threshold rate, dendrites start to nucleate along the coated outer edges as well, so that dendrites penetrate and advance through both the coated and uncoated areas. However, no dendritic avalanches cross the coat boundary yet, even as the uncoated area is fully penetrated by dense dendritic avalanches. Only at even higher rates, above some third threshold ramping rate, do dendrites manage to cross the inner coat boundary. Just like at the slow ramping rates, the dendrites that cross from the uncoated area into the coated area do so through what appears to be a new dendritic nucleation; the new dendrites have "roots" along the inner coat edge and do not seem to continue existing branches in the uncoated area (but rather appear sometimes with anti-dendrites trails in the uncoated area).

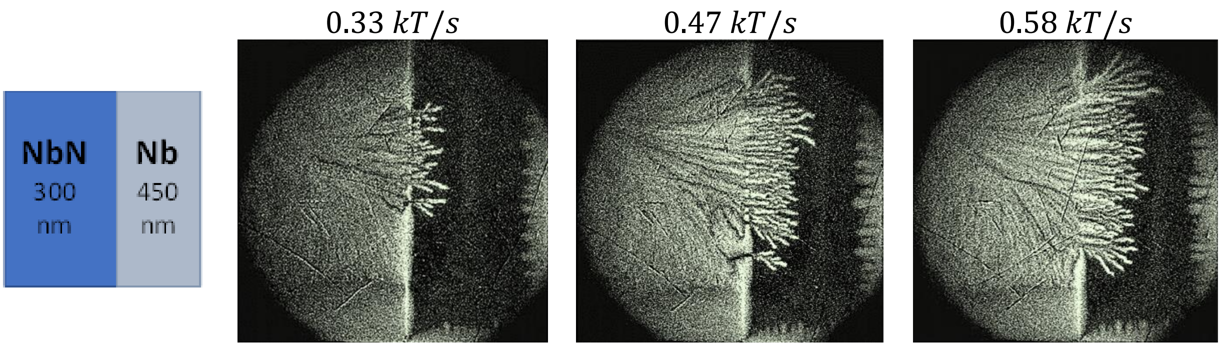

Figure 3.2.11: Effect of the field ramping rate on the coat edge dendrites in sample C_{II}, all images were taken at $T = 6.4\ K$ and $\mu_0 H = 7\ mT$.

By further focusing on the dendrites that enter the inner coat edge and studying the effect of increasing ramping rates on them, we can see that nucleation is not the only way for dendrites to cross the inner boundary, as can be seen in the MO images in figure 3.2.11 above. At low ramping rates, the dendrites indeed cross only through nucleation, as we have seen until now. However, as the ramping rate increase further, more dendrites manage to enter the coated area through the inner coat edge. Some of those dendrites are still nucleated dendrites, but some seem to be a continuation of existing dendritic branches in the uncoated area; they do not have a "root" and we can detect a positive dendritic branch they continue from the uncoated area. The number of those continuing branches increase with increasing ramping rate, but there are always a few dendrites that still advance through nucleation.

We can also see in the images in figure 3.2.11 the continuing dendrites tend to gather around the sample center, where the dendritic branches from the uncoated area reach the inner edge almost perpendicularly, while the nucleating dendrites appear further from the center, where the branches from the uncoated area reach the boundary at a large incident angle. In the discussion chapter we will delve deeper into the meaning of those continuing dendrites for the identification of the new types of dendrites and the way in which those types can move between the different areas of the coated samples.

Lastly, we searched again for the lowest field value at a given ramping rate to cause an avalanche, while distinguishing the sample's areas, thus finding the coated and uncoated threshold fields of sample C_{II}. Due to difficulties with the experiment setup, our measurements suffer limited data points, making the conclusion of overall trends difficult. However, we can still point to some clear repeating behaviors.

The first behavior is that at a given field, the ramping rate threshold of the coated area is always higher than the threshold rate of the uncoated area. Meaning that the superconducting coat layer do offer a suppression method against dendrites caused by fast ramping fields. For example, at $T = 4.9\ K$, the threshold field of the uncoated area reached a value of $\mu_0 H_{th}^1 = 4\ mT$ at ramping rate of $\mu_0 \dot{H} = 0.04\ kT/s$ while the threshold field of the coated area reached it only at the higher rate of $\mu_0 \dot{H} = 0.44\ kT/s$. Similarly, at $T = 5.5\ K$, the threshold field of the uncoated area reached $\mu_0 H_{th}^1 = 5\ mT$ at ramping rate of $\mu_0 \dot{H} = 0.36\ kT/s$ while the threshold field of the coated area reached it at $\mu_0 \dot{H} = 0.59\ kT/s$. These results can be understood by considering the additional flux shielding the Nb coat offer the sample, effectively increasing the sample thickness, and therefore increasing the threshold field as well.

We can also say, with caution, the threshold fields of both areas seem to decrease with increasing ramping rate. for example, at $T = 5.5\ K$, the uncoated threshold field decreases from $6\ mT$ to $4\ mT$ with ramping rate that increases from $0.3\ kT/s$ to $0.38\ kT/s$. This result fits the known theoretical models we presented in the introduction; higher ramping rates cause larger electrical fields and in turn generate greater heat in the sample, leading to the decrease in the threshold field required to induce the first avalanche. Since both the underlayer NbN and the coating Nb are superconducting, the effect of the ramping rate on both areas is essentially the same, the only difference being the coated area consisting of the two layers instead of only one (which as we mention in the previous paragraph, helps the thermomagnetic stabilization).

Finally, the different critical temperatures of the Nb (9 K) and NbN (13.8 K) layers allow the possible investigation of the structure transition from superconductor-coated superconductor into a metal-coated superconductor structure with increasing temperature; At low temperatures above T_{th} and under fast ramping fields, as is seen from the MO image at 7.5 K in figure 3.2.12 below, the Nb layer is still superconducting, and dendritic avalanches still nucleate both along the outer Nb-coated edges and along the inner Nb coat border as was observed and discussed for temperatures below T_{th}. We can also see that the dendrites in the Nb-coated area still exhibit a different typical shape than that of the dendrites in the uncoated NbN area and the dendrites that nucleate along the Nb coat inner edge do so through new nucleation.

However, as the sample temperature increase further above T_{th} and near the Nb critical temperature, less dendrites nucleate along the Nb-coated area edges, until all dendrites seem to nucleate only along the uncoated NbN edges and the Nb layer becomes normal conducting at 9 K, as can be seen from its MO image in figure 3.2.12. Unfortunately, as we increased the sample temperature towards 9 K, the MO images quality decreased, making the conclusion of additional clear behaviors of the dendritic avalanches at those temperatures and at temperatures above 9 K very difficult.

In the discussion chapter we will further compare the avalanches' suppression of the superconductor-coated samples we have shown here and the suppression of the metal-coated sample we presented previously. we will discuss the contribution of each method and its suppression mechanism and conclude the better suppression method.

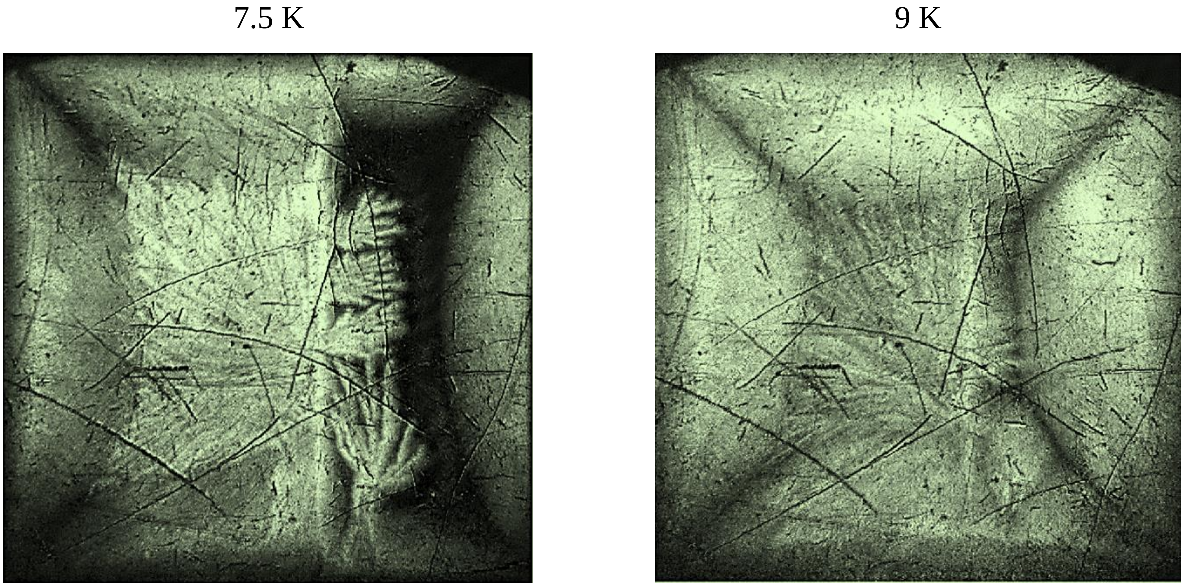

Figure 3.2.12: MO images of sample C_{II} at high temperatures at field of 5 mT and at ramping rate of 0.62 kT/s.

4. Discussion

4.1. Comparison of the metal- and the superconductor-coat suppression under fast ramping rates

Our main goal in this work was to compare the suppression of the metal and superconducting coating methods, under fast ramping magnetic fields. Our initial assumption was that since superconducting films lose their stability with increasing ramping rates of the external field, adding another superconducting film to the underlayer superconductor will not help beyond some small contribution of increasing the effective thickness of the sample. A metallic coating layer, on the other hand, resist the fast entry of the magnetic flux to a larger degree as the ramping rate increases, and can therefore offer a stronger contribution for the avalanche suppression. Taking into account the additional contribution of the Cu layer as a heat-sink as well, we expected the Cu-coating to give a better suppression than the Nb-coating.

Using the suppression coefficient we introduced in the introduction chapter, $S \equiv \frac{d_m \sigma_m}{d_s \sigma_{sn}}$, we can compare the assumed suppression of samples A_I and A_{III}, with their 150 nm and 450 nm Cu coat, respectively. d_m, σ_m being the metal layer's thickness and conductivity, d_s, σ_{sn} being the superconductor's thickness and its normal-state conductivity and $S \gg 1$ corresponds to a good avalanche suppression. Treating the Nb coat layer above its T_C, where it is no longer superconducting, we can express its suppression coefficient as well, where we assumed the Nb coat to exhibit better suppression as a normal-conductor than as a superconductor. We can therefore see again how the Cu layer is expected to offer the better suppression for a given thickness. The calculated S coefficients for the different samples are presented in table 4.1.1 below.

Sample	Coating layer	S
A_{II}	150 nm Cu	1310
A_{III}	450 nm Cu	3950
B_{II}	300 nm Nb	240
C_{II}	450 nm Nb	359

Table 4.1.1: Coating thickness and calculated suppression coefficients of the different samples.[10]

The suppression coefficients of the different samples can also help understanding the big difference in the suppression we observed between samples A_{II} and A_{III}. The thicker Cu-coating layer of layer A_{III} allowing larger induced eddy currents and thus offering a better suppression (by factor of ~3) than the thinner Cu coat layer of sample A_{II}. The same can be said on the Nb-coated samples, B_{II} and C_{II}.

Using the threshold values of the samples under fast ramping fields as an indication of the samples' instability regime, we gathered in figure 4.1.2 the experimental threshold values of both the Cu-coated sample A and the Nb-coated sample C, before and after each coating process. In this graph we also made the distinction between the threshold fields of the coated and uncoated areas in the coated samples, though in the case of sample A_{III}, both values are identical and thus overlap. Both sample A_{III} and sample C_{II} had the same coating thickness of 450 nm.

First of all, we can see from the comparison in figure 4.1.2 below that both bare samples' threshold fields show a very similar dependency on the ramping rate, and can therefore conclude both samples to have a similar initial instability regime[11], making the comparison between the coated results meaningful.

We can also see, quite surprisingly, that the Nb-coated sample suppress the thermomagnetic instabilities to a much larger degree than the Cu-coated sample, its threshold values being higher by few mili-Teslas, even the threshold fields of the uncoated areas. This result refutes our initial assumption, as the same coating thickness of Nb helps the stabilization of the sample much more than the Cu coat. We also saw in the results chapter that the Nb coat stops the advancing dendrites

[10] The typical conductivities were taken as $\sigma_{Cu} = 20 \cdot 10^{6}(\Omega \cdot cm)^{-1}$, $\sigma_{NbN} = 7.6 \cdot 10^{3}(\Omega \cdot cm)^{-1}$, $\sigma_{Nb} = 1.82 \cdot 10^{6}(\Omega \cdot cm)^{-1}$.

[11] This conclusion is also supported by the observation of their similar threshold temperature under slow ramping field, as was explained in the results chapter.

completely up to a threshold ramping rate, dendrites entering the coated area only above it, while the Cu coat allowed a few dendritic branches to enter the coated area for all ramping rates. Overall, the conclusion from this comparison is that the coating of a superconducting film by an additional superconducting layer is the better method to increase its stability against fast ramping magnetic fields.

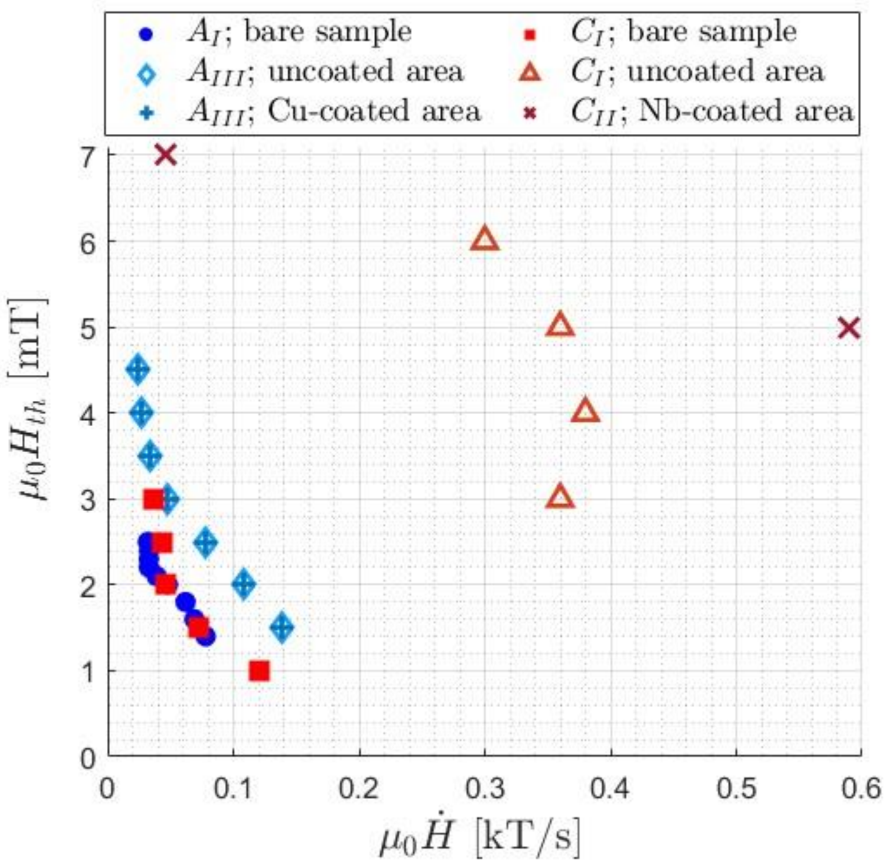

Figure 4.1.2: Comparison of the lower threshold field's, $\mu_0 H_{th}^1$, dependency on the magnetic field rising rate, $\mu_0 \dot{H}$, between the bare samples A_I and C_I and the coated samples A_{III} and C_{II} at temperature of $T = 5.5\ K$.

This strong suppression can be explained by the shielding currents of the Nb layer, and its effect on the advancing vortices and dendritic avalanches through Lorentz forces, even before they reach the Nb-coated area, while the eddy currents in the Cu coat are induced and affect the moving avalanches only as the avalanches reach and move under the Cu-coated area.

However, unlike the simpler case of the Cu-coating, the Nb-coating introduces additional interesting phenomena regarding the behavior of the dendritic avalanches, which will be discussed separately in the following chapter, 4.2.

4.2. Hybrid and surface dendrites in partially superconductor-coated samples

Focusing on the results of the partially Nb-coated samples we described in section 3.2 (pages 32-45), we can also identify three distinctive types of dendritic avalanches, differentiating in their nucleation edge, their form, and their temperature dependency. For clarity, the differences are organized and presented in table 4.2.1 below:

	#1	#2	#3
Nucleation edge	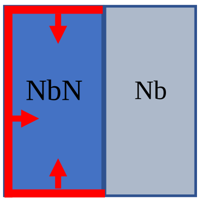	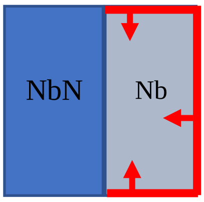	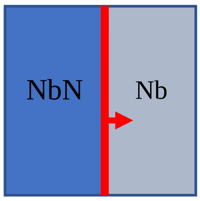
Typical dendritic shape			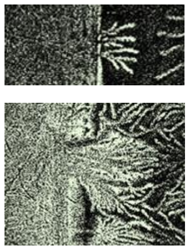
Temperature dependent[12]	✗	✗	✓

Table 4.2.1: an organizing table of the different kinds of dendrites observed in the Nb-coated samples and their characteristics. The representative MO images are of sample C_{II}, the upper and lower images for #3 taken at $4.3K$ and $4.6K$ respectedly.

The clear distinction in the shape of the first and the latter two types of dendrites can be understood by considering the different medium through which each type advances. Previous works on dendritic flux avalanches already showed different superconductors has different typical dendrites (a good and wide comparison is found in the review article [46]). Though no works showed specifically how the superconductor's films parameters determine the shape dendritic avalanches take inside it, one can expect parameters such as the coherence length, its thermal conductivity, pinning centers density, heat capacitance and heat transfer to the substrate all to take part in the determination of the material's typical avalanches' shape. We can therefore understand why the first type of dendrites, regular

[12] In the measured temperature range of the experiment.

dendrites that advance through the NbN layer only, have a different shape than the second and third types of dendrites that move in the Nb/NbN bilayer area because of their different medium.

This explanation, however, is not enough to explain the distinction between the second and the third types of dendrites, since both types appear in the same coated area and are therefore expected to be affected by the same medium's parameters. For that reason, another mechanism differentiating those two types of dendrites is required, specifically to explain the different dependency in temperature they show.

By considering the results presented in figure 3.2.2, where we showed the smooth flux penetration depth into the Nb-coated area varies strongly with increasing temperature (while the penetration depth into the uncoated NbN area remained quite constant), we can present such a mechanism and explain the strong temperature dependency of the third type of dendrites as well; the Nb layer is closer to its critical temperature than the NbN underlayer is, and so it is much more sensitive to changes in temperature. We use this explanation from here onwards to associate strong temperature dependency in our results to the Nb layer, while associating weaker temperature dependency to the NbN underlayer (an association that is also supported by the fact the regular NbN dendrites indeed do not show strong temperature dependency).

Additionally, taking into account the fact the third type of dendrites nucleates along the inner edge of the Nb coat layer, at the center of the sample where we would not have expected to have any nucleation whatsoever, we can identify the third type of dendrites as surface dendrites that are created in the coating Nb layer only. The magnetic shielding of the Nb coat layer stops the dendrites from the uncoated NbN and bends the external magnetic field lines along the inner Nb edge so that a magnetic pressure is built at the Nb edge, eventually leading to the nucleation of dendrites in the coat layer that are highly sensitive to the Nb temperature, as exhibited by their form at increasing temperatures.

Lastly, the second type of dendrites can be identified now as hybrid dendrites that exist in both the NbN underlayer and the Nb coat layer and are affected by both. This identification is supported by these dendrites having weak temperature dependency (like the regular NbN dendrites) and by the different shape those dendrites had in samples B_{II} and C_{II}, as was presented in figure 3.2.7. In sample B_{II}, with 300 nm NbN and 300 nm Nb coating, the hybrid dendrites were closer in shape to the regular NbN dendrites than the hybrid dendrites in sample C_{II} with the 300 nm NbN and the thicker 450 nm Nb coating. We can therefore see that indeed both the NbN and the Nb layer affect the hybrid dendrites.

The identification of the hybrid dendrites as such can also be supported by images, such as in figure 3.2.8, where dendrites advance from the coated area into the uncoated area without any nucleation and with clear propagation of existing branches, with only their shape changing upon crossing from area to area. We can understand this behavior as the hybrid dendrites continuing as normal NbN dendrites by "removing" their tops in the Nb layer as they cross into the uncoated NbN area.

An important point to stress here, however, is that while the hybrid dendrites occupy both layers, due to the large thickness of the Nb and NbN layers in our samples, proximity effects at the interface are neglectable, and we expect each layer to keep its own superconducting parameters. Meaning that our Nb/NbN hybrid dendrites exist simultaneously in two different superconductors and need to balance the preference of each layer for a specific dendritic shape. This situation is quite different to the one we brought in the introduction chapter [35], where a hybrid Nb/NbN bilayer sample was studied and showed improved thermomagnetic stability, explained through proximity effects due to the small thickness of the sample's layers.

To summarize, we used the different nucleation edge, shape and temperature dependency to differentiate between the three different types of dendrites we observed in our superconductor-coated superconductor samples. By explaining the differences and their causes we identified two new, previously unknown, types of dendrites – hybrid dendrites that exist in the Nb/NbN bilayer and surface dendrites that are created in the Nb coat layer only. The discovery of those new types of dendrites is of great importance, as it provides new understanding, as well as many new open questions, regarding the formation and behavior of dendritic avalanches in complex layered superconducting samples.

Identifying these dendrites as three different types, we can now further discuss each type's threshold field and thermomagnetic instability; the threshold fields of each dendrite type in relation to the external field and to local field are presented in figure 4.2.2 below.

(a) (b)

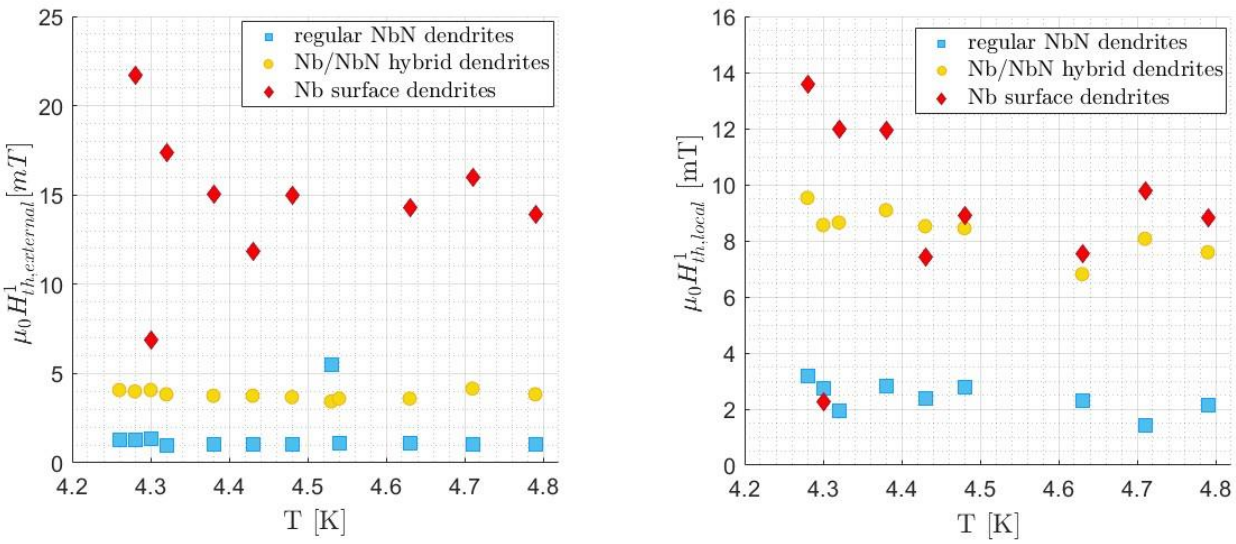

Figure 4.2.2: a) the external threshold fields required for the first nucleation of each dendrites type vs temperature. b) the local threshold fields (obtained through MO image processing) required for each dendritic type first nucleation vs temperature.

As can be seen from figure 4.2.2a, the regular NbN dendrites has the lowest threshold field and are the easiest to induce by applying an external field. After them the hybrid Nb/NbN dendrites have higher threshold field, as inducing them is harder, the Nb-coated NbN area being more stable against thermomagnetic instabilities. And lastly, the Nb surface dendrites has the highest threshold field, as they are the hardest to induce. We can also see that while the threshold fields of the regular and hybrid dendrites remain quite constant with temperature, the surface dendrites' threshold field decreases with increasing temperature, a surprising result, as the lower threshold field of regular dendrites increases with temperature.

In order to verify the decrease of the threshold fields of the surface dendrites, as well as the order of threshold fields, we continued to process the MO images of the sample, and to extract the local fields to induce the different dendrites along the different edges. This way, the demagnetization of the different areas is taken into account, as well as the magnetic shielding of the coat layer by the NbN underlayer, the processed results shown in figure 4.2.2b. Here, we can see again that the coated area is much more stable than the uncoated area, the local threshold field of the hybrid dendrites is significantly higher than the threshold field of the regular ones. Meaning that the formation of such a hybrid dendrite requires larger energies, through stronger magnetic pressure on the sample edge.

We can also see that, even considering the local field, the surface dendrites' threshold fields decrease with increasing temperature. Such odd behavior can perhaps be explained by the coat layer shielding weakening with increasing temperature, allowing field lines to penetrate deeper into the Nb coat layer and bringing it closer to the case of hybrid dendrites.

Lastly, we can see that at low temperature, the surface dendrites have the highest local threshold fields, meaning they require large energies to nucleate, and with increasing temperatures, the energies required for the nucleation decrease, making the nucleation of the surface dendrites easier, until it reaches values such as the hybrid dendrites.

The identifications and observations we made here are further supported by additional COMSOL simulations we performed on such superconductor-coated structures. The first initial simulation is a simple one, made by Itay Garofy from our group, shows the magnetic lines bending and the perpendicular field component on the sample, as can be seen in figure 4.2.3 below. This simulation was executed with the assumption of the coat layer being of the same material as the underlayer (the material thickness step regarded as a coat layer), while neglecting the flux vortices in the sample and using a simple demagnetization modeling for it. Though the simulation simple premise, we can still use it for some important conclusions.

The first conclusion we can extract from the simulation results presented in figure 4.2.3 is the fact that a high magnetic field is indeed built along the inner coat edge, but only at the coat layer edge and height, while at the underlayer height no such field is present. This observation supports the claim of surface dendrites' nucleation in the coat layer only, as only the coat layer feels the magnetic pressure on it.

(a)

(b)

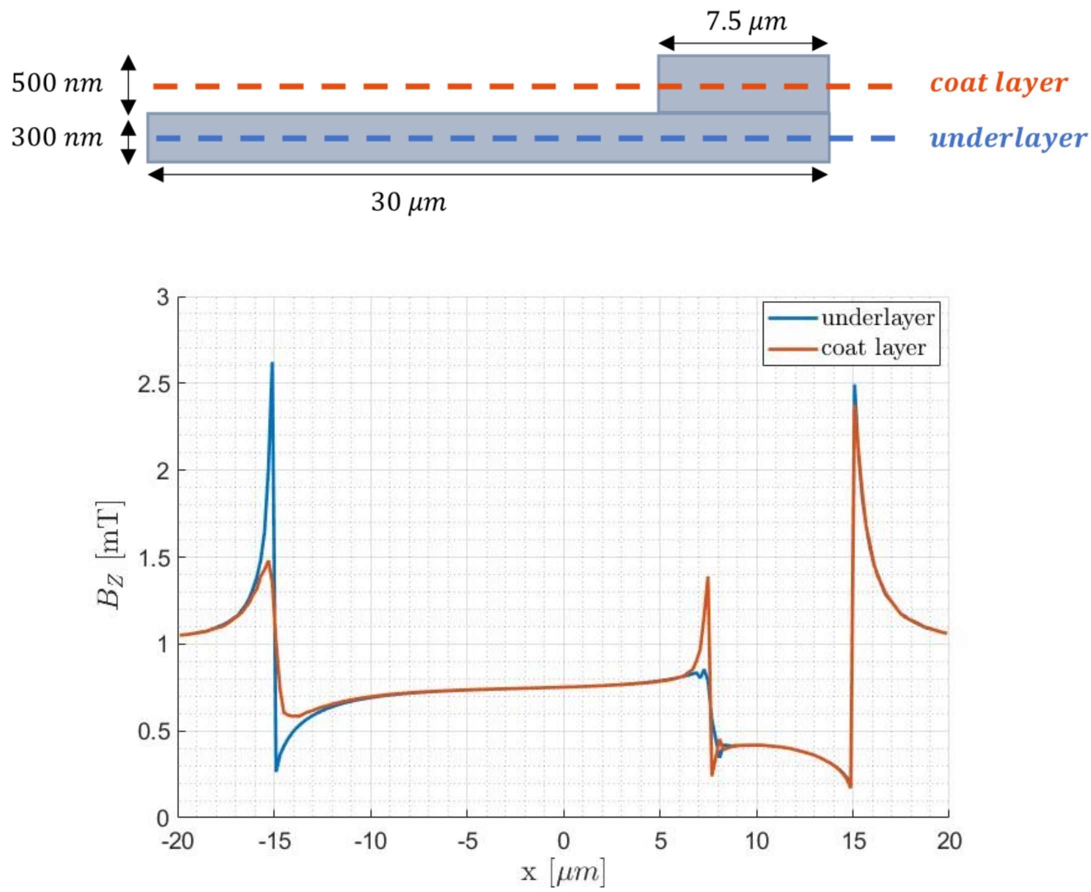

Figure 4.2.3: a) schematic of the modeled superconducting sample with step in thickness. b) COMSOL simulated results of perpendicular magnetic field across a and at different height lines.

A second important observation we can make is of the values the magnetic field reaches along each edge of the sample and the relation between its magnitudes there to the threshold fields of the different dendrites in the sample and their nucleation order. We can see that the highest field is along the uncoated underlayer edge, because of the strong demagnetization there, followed by the coated bilayer edge and then by the inner coat edge. This order is the same order we have seen for the nucleation of the dendrites in our experimental results; the threshold field for the regular uncoated NbN dendrites is the lowest, the hybrid Nb/NbN dendrites have higher threshold fields, and finally the surface Nb dendrites have even higher threshold fields, as is shown in figure 4.2.2 above. The stronger the demagnetization is along an edge, the higher the local field there, and the lower external field required to cause the first nucleation there is, resulting in the nucleation order we have described and seen in our results.

Finally, a more accurate simulation, taking into a greater account the superconducting characterizations, was performed by Dr. Yasha Nikulshin from our group, as is shown in figure 4.2.4 below. Here, the banding of the magnetic field is even clearer, as are the field lines that make a turn inside the coat layer; entering and exiting the coat layer without entering the underlayer below, hence supporting even further the existence of the surface dendrites in the Nb coat layer we have identified.

We can also see the perpendicular field magnitudes along each edge and see again the uncoated edge having the highest field corresponding with the lowest threshold field of the regular uncoated dendrites, followed by lower field on the coated edge corresponding to the higher threshold fields of the hybrid dendrites, followed lastly by the lowest field along the coat inner edge corresponding to the highest threshold field of the surface dendrites.

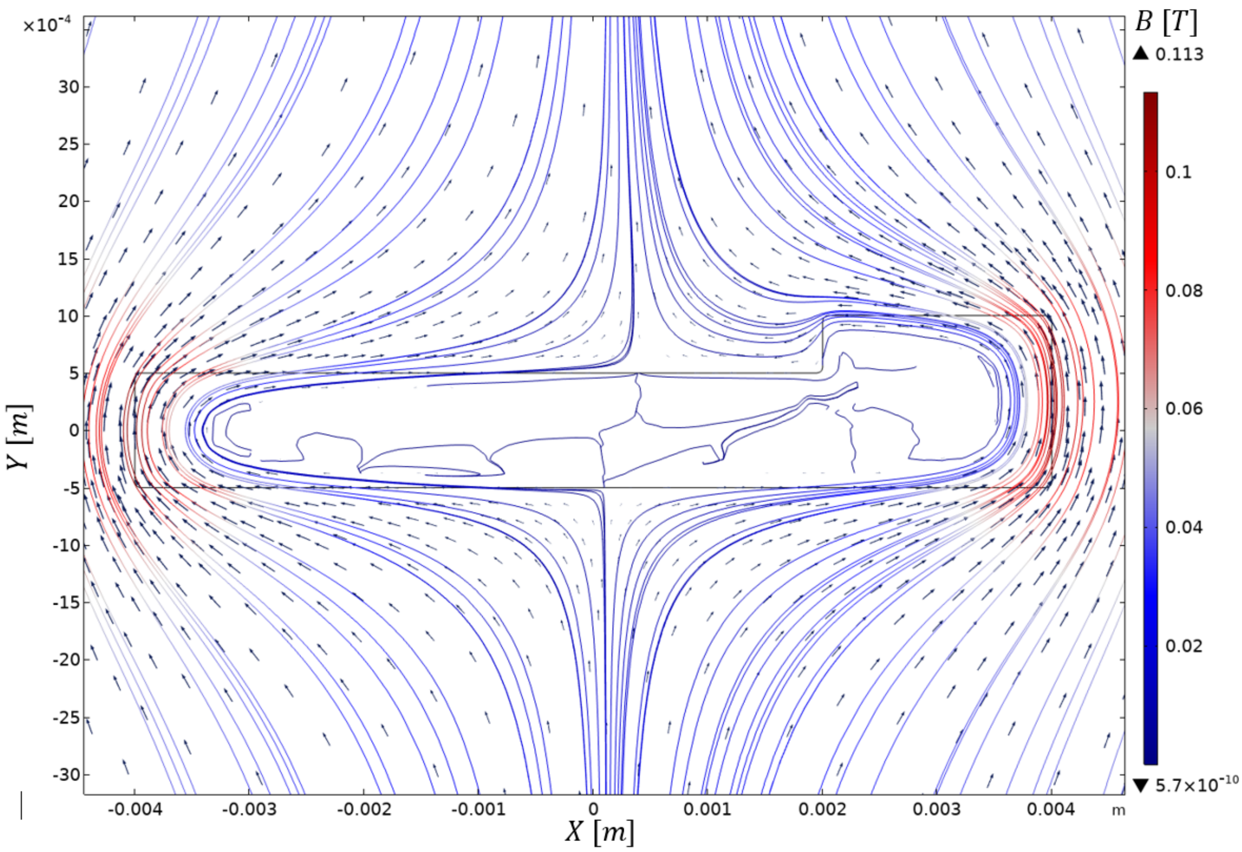

Figure 4.2.4: Simulated results of the magnetic field lines and magnitude for a superconducting sample with thickness step.

5. Conclusions

In this dissertation, we presented our study of the suppression of dendritic flux avalanches, generated by fast ramping magnetic fields, in metal-coated and superconductor-coated superconducting samples. For this purpose, partially Cu-coated NbN and partially Nb-coated NbN samples were fabricated and investigated, using our unique ultra-fast MOI system. The suppression of each coating method was then studied by observing the dendritic avalanches in each sample from the resulting MO images and by measuring the threshold fields of the samples' thermomagnetic instability.

The partially Cu-coated NbN sample's results showed the suppression of the dendritic avalanches by eddy currents induced in the metal-coat due to the moving flux, under fast ramping fields. The vortex motion damping by the eddy currents suppresses completely the initial build-up of the avalanche event, and prevent dendritic avalanches from nucleating along the sample coated edge, for all of the measured ramping rates. In the case where dendritic avalanches nucleate along the sample's uncoated edge and advance towards the coated area, electromagnetic braking by the eddy currents stops most of the branches at the boundary between the areas. While few energetic branches do manage to penetrate into the coated area, they, too, are stopped shortly after by the electromagnetic braking. The number of dendritic branches that manage to enter the coated area, as well as the depth to which they manage to advance to, are dependent on the magnetic field ramping rate; as the ramping rate increases, more energetic dendritic branches advance through the sample, overcoming the electromagnetic braking and entering the coated area to a much deeper distance. The metal-coat suppression is therefore dependent on the field ramping rate, as is also shown through the thermomagnetic instability threshold fields, the suppression efficiency decreasing with increasing ramping rates.

In the Nb-coated NbN samples, on the other hand, we showed dendrites do nucleate even along the coated edges. But, due to the increase of the effective thickness and the additional shielding currents in the Nb coat, the threshold field and threshold ramping rate of the dendrites along the coated edges are higher than the threshold values of dendrites in the uncoated area. Furthermore, all dendritic branches that reach the coat boundary from the uncoated area are stopped completely and abruptly, only managing to penetrate the coated area above a threshold field and a threshold ramping rate, higher than the threshold values of both the coated and uncoated areas. Additionally, due to their exact formation, we identified the entry of dendrites through the inner coat edge of the Nb as new avalanche nucleation.

Based on these results and supporting simulations, we deduced the existence of two new and distinct types of dendrites: Hybrid dendrites, that occupied both the Nb and NbN layers, and were affected by both. And surface dendrites, that were created at the Nb coat layer only, and not in the NbN underlayer. The hybrid dendrites showed a dendritic formation that is affected by both Nb and NbN layers and weak temperature dependency, while the surface dendrites show stronger sensitivity for temperature variations. Each type of dendrites has its own threshold field and threshold ramping rate, the surface dendrites having higher threshold values than the hybrid dendrites, and both having higher threshold values than the regular NbN's. Interestingly, though, the threshold field of the surface dendrites decreases with increasing temperature – a unique dependency that requires further explanation. We also showed evidence for the transformation of regular NbN dendrites to Nb/NbN hybrid dendrites, and vice versa, the first case occurring only in cases of extremely fast ramping rates, due to the energy needed for the increase of the regular NbN dendrite's 'height' upon becoming an Nb/NbN hybrid dendrite.

Finally, from the comparison of the metal-coated and superconductor-coated samples' threshold fields, we saw the superconductor-coat offers a significantly better suppression of dendritic avalanches generated by fast ramping magnetic fields, its threshold fields being ~2 times higher than the threshold fields of the metal-coated samples.

6. References

[1] A. A. Abrikosov, "The magnetic properties of superconducting alloys," *J. Phys. Chem. Solids*, vol. 2, no. 3, pp. 199–208, Jan. 1957, doi: 10.1016/0022-3697(57)90083-5.

[2] T. H. Johansen *et al.*, "Dendritic magnetic instability in superconducting MgB 2 films," *Europhys. Lett.*, vol. 59, no. 4, pp. 599–605, Aug. 2002, doi: 10.1209/epl/i2002-00146-1.

[3] E. Altshuler and T. H. Johansen, "Colloquium : Experiments in vortex avalanches," *Rev. Mod. Phys.*, vol. 76, no. 2, pp. 471–487, Apr. 2004, doi: 10.1103/RevModPhys.76.471.

[4] C. P. Bean, "Magnetization of high-field superconductors," *Rev. Mod. Phys.*, vol. 36, no. 1, pp. 31–39, 1964, doi: 10.1103/RevModPhys.36.31.

[5] M. R. Wertheimer and J. le G. Gilchrist, "Flux jumps in type II superconductors," *J. Phys. Chem. Solids*, vol. 28, no. 12, pp. 2509–2524, Jul. 1967, doi: 10.1016/0022-3697(67)90038-8.

[6] Y. Yeshurun, A. P. Malozemoff, and A. Shaulov, "Magnetic relaxation in high-temperature superconductors," *Rev. Mod. Phys.*, vol. 68, no. 3, pp. 911–949, May 1996, doi: 10.1016/S0375-9601(99)00140-1.

[7] D. V. Denisov *et al.*, "Onset of dendritic flux avalanches in superconducting films," *Phys. Rev. Lett.*, vol. 97, no. 7, p. 077002, 2006, doi: 10.1103/PhysRevLett.97.077002.

[8] E. H. Brandt and M. Indenbom, "Type-II-superconductor strip with current in a perpendicular magnetic field," *Phys. Rev. B*, vol. 48, no. 17, pp. 12893–12906, 1993, doi: 10.1103/PhysRevB.48.12893.

[9] A. J. Qviller *et al.*, "Irreversibility of the threshold field for dendritic flux avalanches in superconductors," *Phys. C Supercond.*, vol. 470, no. 19, pp. 897–900, Oct. 2010, doi: 10.1016/j.physc.2010.02.066.

[10] F. Colauto, M. Motta, and W. A. Ortiz, "Controlling magnetic flux penetration in low-TC superconducting films and hybrids," *Supercond. Sci. Technol.*, vol. 34, no. 1, p. 013002, Jan. 2021, doi: 10.1088/1361-6668/abac1e.

[11] J. I. Vestgården, D. V. Shantsev, Y. M. Galperin, and T. H. Johansen, "Flux penetration in a superconducting strip with an edge indentation," *Phys. Rev. B*, vol. 76, no. 17, pp. 1–5, 2007, doi: 10.1103/PhysRevB.76.174509.

[12] U. Bolz, B. Biehler, D. Schmidt, B. U. Runge, and P. Leiderer, "Dynamics of the dendritic flux instability in YBa2Cu 3O7-δ films," *Europhys. Lett.*, vol. 64, no. 4, pp. 517–523, 2003, doi: 10.1209/epl/i2003-00261-y.

[13] B. Biehler, B. U. Runge, P. Leiderer, and R. G. Mints, "Ultrafast magnetic flux dendrite propagation into thin superconducting films," *Phys. Rev. B*, vol. 72, no. 2, pp. 1–5, 2005, doi: 10.1103/PhysRevB.72.024532.

[14] M. Baziljevich, E. Baruch-El, T. H. Johansen, and Y. Yeshurun, "Dendritic instability in YBa2Cu3O7-δ films triggered by transient magnetic fields," *Appl. Phys. Lett.*, vol. 105, no. 1, pp. 1–5, 2014, doi: 10.1063/1.4887374.

[15] E. Baruch-El *et al.*, "Magnetic flux instability in NbN films exposed to fast field sweep rates," *Supercond. Sci. Technol.*, vol. 31, no. 10, 2018, doi: 10.1088/1361-6668/aadacb.

[16] E. Baruch-El, M. Baziljevich, B. Y. Shapiro, T. H. Johansen, A. Shaulov, and Y. Yeshurun, “Dendritic flux instabilities in YBa2Cu3O7-x films: Effects of temperature and magnetic field ramp rate,” *Phys. Rev. B*, vol. 94, no. 5, pp. 2–7, 2016, doi: 10.1103/PhysRevB.94.054509.

[17] M. Motta *et al.*, “Flux avalanches triggered by AC magnetic fields in superconducting thin films,” *Phys. C*, vol. 479, pp. 134–136, 2012, doi: 10.1016/j.physc.2011.12.030.

[18] E. Baruch-El, M. Baziljevich, T. H. Johansen, J. Albrecht, A. Shaulov, and Y. Yeshurun, “Dendritic flux instability in MgB2 films above liquid hydrogen temperature,” *Supercond. Sci. Technol.*, vol. 31, no. 2, p. 025005, Jul. 2018, doi: 10.1088/1361-6668/aa9f41.

[19] E. H. Brandt, “Electric field in superconductors with rectangular cross section,” *Phys. Rev. B*, vol. 52, no. 21, pp. 15442–15457, Dec. 1995, doi: 10.1103/PhysRevB.52.15442.

[20] J. I. Vestgården, Y. M. Galperin, and T. H. Johansen, “Oscillatory regimes of the thermomagnetic instability in superconducting films,” *Phys. Rev. B*, vol. 93, no. 17, pp. 1–4, May 2016, doi: 10.1103/PhysRevB.93.174511.

[21] Y. B. Kim, C. F. Hempstead, and A. R. Strnad, “Magnetization and critical supercurrents,” *Phys. Rev.*, vol. 129, no. 2, pp. 528–535, 1963, doi: 10.1103/PhysRev.129.528.

[22] F. L. Barkov *et al.*, “Local threshold field for dendritic instability in superconducting MgB2 films,” *Phys. Rev. B*, vol. 67, no. 6, p. 064513, Feb. 2003, doi: 10.1103/PhysRevB.67.064513.

[23] M. Baziljevich, D. Barness, M. Sinvani, E. Perel, A. Shaulov, and Y. Yeshurun, “Magneto-optical system for high speed real time imaging,” *Rev. Sci. Instrum.*, vol. 83, no. 8, pp. 1–8, 2012, doi: 10.1063/1.4746255.

[24] M. Baziljevich, A. V. Bobyl, D. V. Shantsev, E. Altshuler, T. H. Johansen, and S. I. Lee, “Origin of dendritic flux patterns in MgB2 films,” *Phys. C*, vol. 369, pp. 93–96, 2002, doi: 10.1016/S0921-4534(01)01226-6.

[25] J. Brisbois *et al.*, “Flux penetration in a superconducting film partially capped with a conducting layer,” *Phys. Rev. B*, vol. 95, no. 9, pp. 1–8, 2017, doi: 10.1103/PhysRevB.95.094506.

[26] V. V. Yurchenko *et al.*, “Suppression of magnetic flux avalanches and recovery of the critical state in superconducting NbN films,” *arXiv Prepr.*, Nov. 2012, [Online]. Available: http://arxiv.org/abs/1211.3787.

[27] P. Mikheenko, J. I. Vestgården, S. Chaudhuri, I. J. Maasilta, Y. M. Galperin, and T. H. Johansen, “Metal frame as local protection of superconducting films from thermomagnetic avalanches,” *AIP Adv.*, vol. 6, no. 3, p. 035304, Mar. 2016, doi: 10.1063/1.4943549.

[28] J. Brisbois *et al.*, “Classical analogy for the deflection of flux avalanches by a metallic layer,” *New J. Phys.*, vol. 16, pp. 1–12, 2014, doi: 10.1088/1367-2630/16/10/103003.

[29] J. Albrecht, A. T. Matveev, M. Djupmyr, G. Schütz, B. Stuhlhofer, and H.-U. Habermeier, “Bending of magnetic avalanches in MgB2 thin films,” *Appl. Phys. Lett.*, vol. 87, no. 18, p. 182501, Oct. 2005, doi: 10.1063/1.2123395.

[30] P. Mikheenko, T. H. Johansen, S. Chaudhuri, I. J. Maasilta, and Y. M. Galperin, “Ray optics behavior of flux avalanche propagation in superconducting films,” *Phys. Rev. B*, vol. 91, no. 6, p. 060507, Feb. 2015, doi: 10.1103/PhysRevB.91.060507.

[31] F. Colauto *et al.*, “Suppression of flux avalanches in superconducting films by

electromagnetic braking," *Appl. Phys. Lett.*, vol. 96, no. 9, pp. 1–3, 2010, doi: 10.1063/1.3350681.

[32] J. I. Vestgården, Y. M. Galperin, and T. H. Johansen, "The thermomagnetic instability in superconducting films with adjacent metal layer," *J. Low Temp. Phys.*, vol. 173, no. 5–6, pp. 303–326, 2013, doi: 10.1007/s10909-013-0899-1.

[33] J. I. Vestgården, P. Mikheenko, Y. M. Galperin, and T. H. Johansen, "Inductive braking of thermomagnetic avalanches in superconducting films," *Supercond. Sci. Technol.*, vol. 27, no. 5, 2014, doi: 10.1088/0953-2048/27/5/055014.

[34] M. Danckwerts, A. R. Goñi, C. Thomsen, K. Eberl, and A. G. Rojo, "Enhanced vortex damping by eddy currents in superconductor-semiconductor hybrids," *Phys. Rev. Lett.*, vol. 84, no. 16, pp. 3702–3705, 2000, doi: 10.1103/PhysRevLett.84.3702.

[35] L. B. L. G. Pinheiro *et al.*, "Magnetic flux avalanches in Nb/NbN thin films," *Low Temp. Phys.*, vol. 46, no. 4, pp. 365–371, 2020, doi: 10.1063/10.0000868.

[36] E. Baruch-El, M. Baziljevich, T. H. Johansen, A. Shaulov, and Y. Yeshurun, "Thickness dependence of dendritic flux avalanches in YBa2Cu3O7-x films," *J. Phys. Conf. Ser.*, vol. 969, no. 1, pp. 1–6, 2018, doi: 10.1088/1742-6596/969/1/012042.

[37] Y. Tsuchiya *et al.*, "Flux avalanches in Nb superconducting shifted strip arrays," *Supercond. Sci. Technol.*, vol. 26, no. 9, pp. 1–7, 2013, doi: 10.1088/0953-2048/26/9/095004.

[38] T. Tamegai *et al.*, "Critical states and thermomagnetic instabilities in three-dimensional nanostructured superconductors," *Phys. C Supercond. its Appl.*, vol. 533, pp. 74–79, 2017, doi: 10.1016/j.physc.2016.07.009.

[39] Y. Ivry *et al.*, "Superconductor–superconductor bilayers for enhancing single-photon detection," *Nanotechnology*, vol. 28, no. 43, p. 435205, Oct. 2017, doi: 10.1088/1361-6528/aa8902.

[40] O. M. Chumak, V. V. Chabanenko, V. F. Rusakov, S. V. Vasiliev, F. Pérez-Rodríguez, and A. Nabiałek, "Threshold Field for Runaway Instability of Bilayer Hard Type-II Superconductor," *J. Low Temp. Phys.*, vol. 179, no. 1–2, pp. 75–82, 2015, doi: 10.1007/s10909-014-1230-5.

[41] S. V. Vasiliev, O. M. Chumak, V. V. Chabanenko, F. Pérez-Rodríguez, and A. Nabiałek, "Stability of bilayer superconductors against thermomagnetic avalanche," *Acta Phys. Pol. A*, vol. 126, no. 4A, pp. A84–A87, 2014, doi: 10.12693/APhysPolA.126.A-84.

[42] H. P. Wiesinger, F. M. Sauerzopf, and H. W. Weber, "On the calculation of Jc from magnetization measurements on superconductors," *Phys. C Supercond.*, vol. 203, no. 1–2, pp. 121–128, Dec. 1992, doi: 10.1016/0921-4534(92)90517-G.

[43] D. X. Chen and R. B. Goldfarb, "Kim model for magnetization of type-II superconductors," *J. Appl. Phys.*, vol. 66, no. 6, pp. 2489–2500, 1989, doi: 10.1063/1.344261.

[44] V. V. Yurchenko, T. H. Johansen, and Y. M. Galperin, "Dendritic flux avalanches in superconducting films," *Low Temp. Phys.*, vol. 35, no. 8, pp. 619–626, 2009, doi: 10.1063/1.3224713.

[45] M. S. Welling, R. J. Westerwaal, W. Lohstroh, and R. J. Wijngaarden, "Huge compact flux avalanches in superconducting Nb thin films," *Phys. C Supercond.*, vol. 411, no. 1–2, pp. 11–17, Sep. 2004, doi: 10.1016/j.physc.2004.06.011.

[46] J. I. Vestgården, T. H. Johansen, and Y. M. Galperin, “Nucleation and propagation of thermomagnetic avalanches in thin-film superconductors (Review Article),” *Low Temp. Phys.*, vol. 44, no. 6, pp. 460–476, 2018, doi: 10.1063/1.5037549.

[47] P. Leiderer, J. Boneberg, P. Brüll, V. Bujok, and S. Herminghaus, “Nucleation and growth of a flux instability in superconducting YBa2Cu3O7-x films,” *Phys. Rev. Lett.*, vol. 71, no. 16, pp. 2646–2649, 1993, doi: 10.1103/PhysRevLett.71.2646.

[48] Y. H. Zhou, C. Wang, C. Liu, H. Yong, and X. Zhang, “Optically Triggered Chaotic Vortex Avalanches in Superconducting YBa2Cu3 O7-x Films,” *Phys. Rev. Appl.*, vol. 13, no. 2, pp. 1–7, 2020, doi: 10.1103/PhysRevApplied.13.024036.

7. Appendix: Dendritic avalanches in YBCO sample with step in thickness.

In this appendix we present some partial results of another experiment we conducted, about dendritic avalanches in dual-thickness YBCO samples. These samples were received from Prof. Michael Baziljevich and initially measured by Dr. Elran Baruch-el, with the hope of detecting ray deflection of the dendritic branches upon crossing thickness areas due to the dendrites different thickness-dependent propagation velocity[30]. Some of the results presented in this appendix, in figure 7.3, are from his measurements. Since the results we describe here do not quite fit the scope of this thesis, yet still offer an interesting additional point of view of the overall phenomenon of dendritic avalanches suppression, we include it in this separate section.

Unlike the low-temperature type II thin superconductor films we discussed through this work, high temperature type II superconductors films, such as YBCO, are very stable against thermomagnetic instabilities. In fact, YBCO samples suffer dendritic flux avalanches only under extreme conditions, such as high local heating [48,49] and very high field ramping rates [14]. This stability is considered to be caused by the short coherence length and the strong and dense pinning centers the YBCO offers [36]. Once an avalanche is triggered, however, the extreme local heating of the fast advancing dendrites often irreversibly harm the YBCO sample and leave permanent defects behind [14]. These defects can than act as an easy entry point for the next dendrites due to the high local magnetic field built at such indents[11].

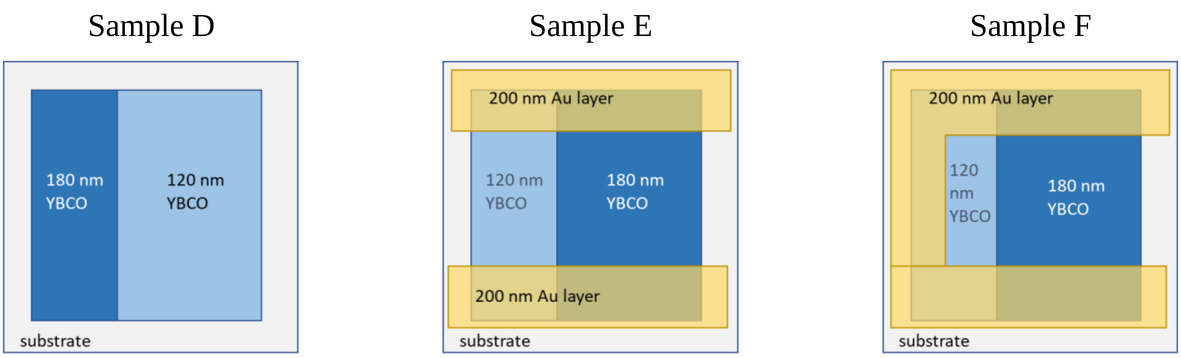

Figure 7.1: Schematics of the three different dual-thickness YBCO samples.

Considering a step in the superconducting film thickness as effectively additional superconducting-coat layer of the same material, we examined the behavior of the thermomagnetic instabilities in YBCO-"coated" YBCO samples under fast ramping magnetic fields. Three samples of $4 \times 4\ mm^2$ sized s-type YBCO films, with 120 nm/ 180 nm dual-thickness, were fabricated by Ceraco on YSZ substrates and with 10 nm CeO2 buffer layer. The samples were later etched and coated with additional 200 nm Au layer for the guidance of the dendritic avalanches towards the step by Dr. Elran Baruch-el, as described in figure 8.1 above. MO measurements of the samples showed their critical temperature to be $T_c \sim 80\ K$. After ZFC, the samples were measured using our fast MOI system at different fields and ramping rates, some representative images of each sample are presented in figures 7.2, 7.3 and 7.4 below.

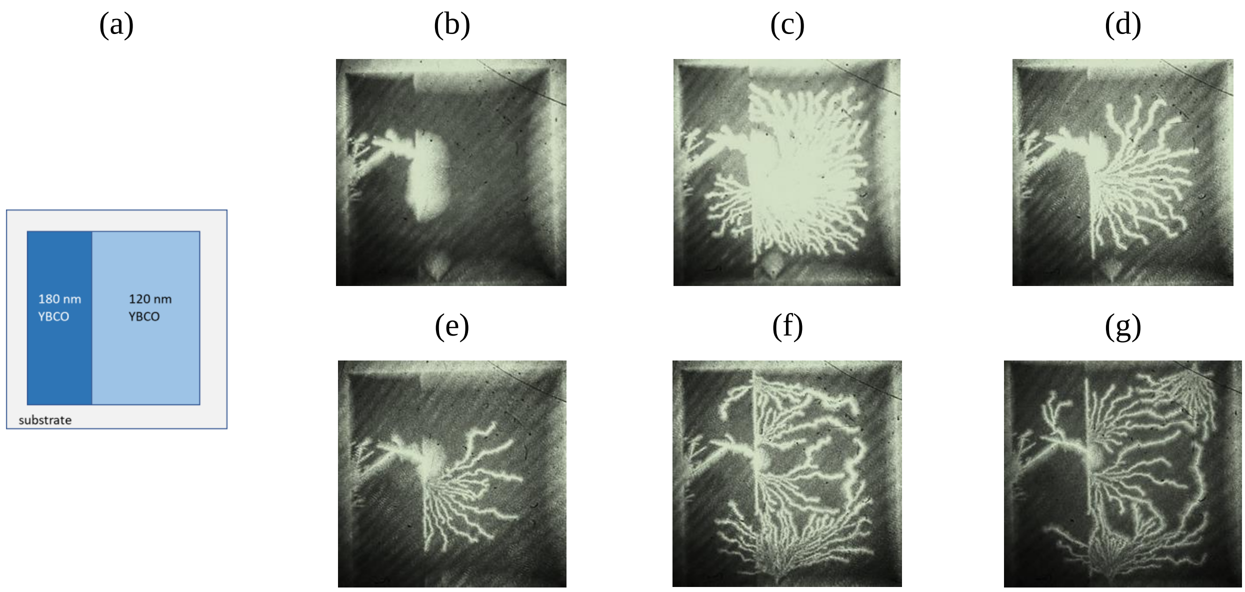

Figure 7.2: a) Schematic of sample D. b-g) MO images of sample D at temperature of $5K$, field of $40\ mT$ and ramping rate of b) $0.14\ kT/s$, c) $0.14\ kT/s$, d) $0.18\ kT/s$, e) $0.34\ kT/s$, f) $0.78\ kT/s$ and g) $1.1\ kT/s$.

As can be seen from the MO images of sample D in figure 7.2, the sample has a large and dominant defect, crossing the thicker area into the center of the sample, at the step edge. This defect was formed by dendritic avalanches during the initial measurements of sample D. From image 7.2b, we can see this defect allows the external field to enter the center of the sample, even as stable and smooth flux penetration at low ramping rates. We can also see the flux penetration depth into the thicker area of the sample is much shallower than the penetration depth into the thinner area. This is due to the larger shielding of the thicker region, and to the larger amount of pinning centers the higher thickness of YBCO offers, making the entry of flux into the thicker area of the sample harder than into its thinner area.

At higher ramping rates, however, the flux entry into the sample is unstable. The defect in the center of the sample still offers an easy entry point, and indeed most dendrites are nucleated at its tip, as can be seen from images 7.2c-g. Only at very high ramping rates, dendrites manage to nucleate at additional edge points of the sample. it is interesting to note here, however, that unlike the case for the low-temperature superconductors we measured through this work, the dendritic avalanches' size in the YBCO samples decrease with increasing ramping rate, but the overall number of dendrites increase.

Because of the large defect leading right to the thickness step boundary, it is hard to determine whether dendrites nucleate along the inner step, forming what we identified as surface dendrites. This identification is made even harder by the "coat" layer being YBCO, with the same superconducting parameters as the underlayer YBCO. Since we used both the different typical shape of the dendrites and their different temperature dependency to identify the formation of the surface dendrites, we cannot identify such dendrites in this sample. though, the dendritic avalanches that enter the thicker area from the step edge in image 7.2c might indeed by a surface dendrite, and in fact, was one of the results that raised our suspicion for the formation of surface dendrites.

(a) (b) (c) (d)

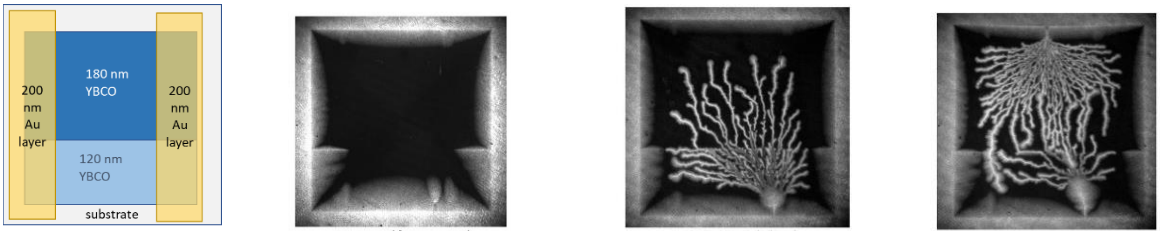

Figure 7.3: a) Schematic of sample E. b) MO image of sample D at temperature of $9K$, field of $40\ mT$ and ramping rate of $2\ mT/s$. c,d) MO images at temperature of $10K$, field of $60\ mT$ and ramping rate of $0.4\ kT/s$ and $0.67\ kT/s$ respectively. The MO images presented here were measured by Dr. Elran Baruch-el.

Similarly, in sample E, we can see again, in image 7.3b above, how the smooth flux penetration is deeper in the thinner area of the sample, and that with increasing ramping rate, more dendrites nucleate along the sample edges and reach deeper inside it. Here, however, all of the dendritic branches that enter the thicker area are a continuation of existing branches in the thinner area, and we could not detect a nucleation along the inner step. However, the step boundary still affects the dendrites greatly, stopping and redirecting many of the dendritic branches that reach the thick area from the thin area, though dendrites that move the opposite way, as shown in 7.3d, cross the step easily.

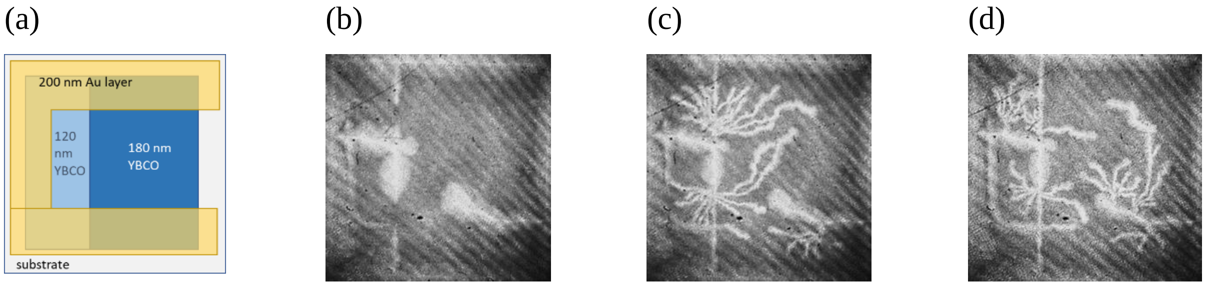

Figure 7.4: a) Schematic of sample F. b-d) MO images of sample D at temperature of $5K$, field of $40\ mT$ and ramping rate of b) $0.24\ kT/s$, c) $0.33\ kT/s$ and d) $1.19\ kT/s$.

Measurements of sample F, presented in figure 7.4 above, show yet again the overall behavior of the dendrites in increasing ramping rate, here however, more dendrites seem to enter the thicker area of the sample, and even seem to enter as new branches, and not a continuation of existing ones from the thin area of the sample, which might hint to them being surface dendrites.

Due to the damages the samples accumulated during the initial measurements, as well as the "coating" layer being of the same material as the underlayer, we could not reach clear conclusions on the behavior of the thermomagnetic instabilities and dendritic avalanches in such samples. However, we suspect some of the dendrites we observed on the thickness step that penetrates the thicker part may actually be surface dendrites, just like we saw in the hybrid Nb-coated NbN samples. This result can be of great importance, as it introduced the possibility of surface dendrites in superconducting sample with thickness step and not only in superconducting hybrid structures. The determination of the existence of surface dendrites could not be made with those samples, since the main observation we used for the determination of nucleation along the coat edge was the clear nucleation of dendrites along the edge and their temperature dependency. Additionally, since the YBCO dendritic avalanches by their nature, has very thin and directional shape, it is quite hard to determine if their entry into the coated area is by nucleation or not.

It is also interesting to note here, that the hybrid dendrites we identified in the Nb-coated NbN sample, do not exist, since the dendrites all over the sample occupy only the YBCO. We could however, suspect that we still have two different types of dendrites here – the normal YBCO dendrites for a thickness of 120 nm, and normal YBCO dendrites for the 180 nm thickness. Since the vortices of the different areas still have different energies due to their length, the interface between the areas is still interesting to study, but the conclusions are not as obvious as in the case of the Nb-NbN samples.

תקציר

מוליכי על דקים מסוג II הנמצאים תחת השפעת שדה מגנטי חיצוני, סובלים במקרים רבים מאי-יציבות מגנטית הבאה לידי ביטוי כמפולות שטף דנדריטיות; פריצות מהירות ומקומיות של שטף מגנטי אל תוך מוליך העל, בצורה של מבנים דנדריטיים מסועפים. מפולות שטף אלו מתרחשות בטמפרטורות נמוכות מטמפרטורת סף אופיינית של הדגם, T_{th}, ובין שדות סף מגנטיים תלויי טמפרטורה המגדירים את תחום אי-היציבות של מוליך העל; שדה הסף התחתון, H_{th}^1, ושדה הסף העליון, H_{th}^2. לאי היציבות המגנטית יכולות להיות השלכות הרות-אסון על אפליקציות מוליכות-על, מכיוון שהן מעלות את טמפרטורת הדגם הלוקאלית אל מעל לטמפרטורה הקריטית של הדגם, T_C, ובמקרים מסוימים אפילו גורמות לנזק בלתי הפיך של הדגם. מסיבות אלו, המחקר של שיטות מיסוך למניעה של מפולות שטף אלו, כמו גם הרחבת תחום היציבות המגנטית של הדגם, הוא חשוב ונצרך. מחקרים שפורסמו לאחרונה, הראו באמצעות טכניקת דימוי מגנטו-אופטית (MOI) איטית, כי ציפוי דגם על-מוליך על ידי שכבה מוליכה נוספת, מתכתית או מוליכת על, עוזר במניעה של מפולות השטף הדנדריטיות האלו. אבל, כאמור, מחקרים אלו בדקו את מיסוך המפולות הדנדריטיות בקצבי עלייה איטיים של השדה המגנטי בלבד ($\sim 1\ mT/s$). כפי שהודגם במסגרת מחקר קודם במעבדה שלנו, קצבי עלייה מהירים של השדה המגנטי פוגעים בתחום היציבות המגנטית של מוליך העל וגורמים להופעת מפולות דנדריטיות גם בטמפרטורות גבוהות מטמפרטורת הסף, ועבור טווח רחב יותר של שדות מגנטיים. כתוצאה מכך תחום אי היציבות של הדגם גדל אף יותר ומשבש אפליקציות מוליכות על באופן חמור יותר. בעקבות כך, לא מספיק לחקור את מיסוך מפולות השטף תחת קצבי עליית שדה איטיים, אלא יש צורך לחקור את שיטות מיסוך מפולות השטף גם בקצבי עליית שדה מהירים. מסיבות ניסיוניות, המחקרים הקיימים מוגבלים לקצבי עליית שדה איטיים, ולכן אין מספיק מידע מחקרי בנושא.

בעבודה זו, אנחנו משתמשים במערכת מגנטו-אופטית מהירה וייחודית שהוקמה אצלנו במעבדה, המאפשרת מדידה של מפולות שטף דנדריטיות הנגרמות עקב קצבי עליית שדה אולטרה-מהירים, למחקר של שיטת מיסוך המפולות על ידי ציפוי דגמים בשכבת מתכת או בשכבה מוליכת על נוספת בקצבי עלייה מהירים. מסיבה זו, חיבור זה יעסוק בשני חלקים ניסויים, כאשר כל חלק נבנה במטרה לחקור את מיסוך מפולות השטף במבנה היברידי שונה.

החלק הראשון עוסק במיסוך המפולות בדגמים מוליכי על המצופים חלקית בשכבה מתכתית, ספציפית בדגם NbN המכוסה חלקית בשכבת נחושת. מדידת המיסוך נעשית על ידי ניתוח תמונות מגנטו-אופטיות של תצורת המפולות הדנדריטיות בדגם, ועל ידי מדידת התלות של שדה הסף התחתון בקצב עליית השדה. התמונות המגנטו-אופטיות של הדגם מראות כי, עבור כל קצבי העלייה שנמדדו במסגרת הניסוי, שכבת הנחושת מונעת לחלוטין נוקליאציה של דנדריטים חדשים על שפת הדגם המצופה בנחושת, בעקבות שיכוך תנועת מערבולות השטף שבמוליך העל על ידי זרמי eddy הנוצרים בשכבת הנחושת. כמו כן, התמונות המגנטו-אופטיות מראות כי בקצבי עלייה נמוכים שכבת הנחושת מונעת ממרבית ענפי המפולות הדנדריטיות המגיעות לגבול בין האזור הלא מצופה והמצופה מלחצות אל האזור המצופה, כאשר מעט הענפים שמצליחים בכל זאת להיכנס אל האזור המצופה נעצרים מרחק קצר לאחר מכן בעקבות בלימה אלקטרומגנטית של זרמי הeddy. אבל, ככל שקצב עליית השדה עולה, המפולות הדנדריטיות הנוצרות הן אנרגטיות יותר, וזרמי הeddy שבנחושת כבר לא מספיקים על מנת לעצור אותן, כך שיותר ענפים דנדריטיים מצליחים לחדור אל אזור הדגם המצופה נחושת ולהתקדם מרחק ארוך יותר לפני שהם נעצרים. למרות זאת, שדות הסף של הדגם מצופה הנחושת גבוהים יותר משדות הסף של דגם הNbN החשוף עבור כל קצבי עליית השדה שנמדדו, כך שציפוי הנחושת אכן משפר את היציבות המגנטית של הדגם ומציע שיטת מיסוך אפשרית, כאשר יעילות המיסוך גבוהה יותר עבור קצבי עליית שדה איטיים ($\sim 0.1\ kT/s$) מאשר עבור קצבי עלייה מהירים.

החלק הניסויי השני, לעומת זאת, עוסק במיסוך המפולות בדגמים מוליכי על המצופים חלקית בשכבת מוליך על נוספת, ספציפית בדגם NbN המכוסה חלקית בשכבת Nb. מדידת המיסוך נעשית על ידי ניתוח תמונות מגנטו-אופטיות של תצורת המפולות הדנדריטיות בדגם, ועל ידי מדידת התלות של שדה הסף התחתון בקצב עליית השדה ובטמפרטורה. התמונות

המגנטו-אופטיות של הדגם מראות כי, בניגוד למקרה של הדגם מצופה הנחושת, בדגם המצופה Nb מפולות דנדריטיות עוברות נוקליאציה גם בשפת הדגם הלא מצופה וגם בשפת הדגם המצופה. אבל, שדה הסף וקצב הסף עבור הדנדריטים הנוצרים על שפת הדגם המצופה גבוהים מערכי הסף של הדנדריטים הנוצרים על שפת הדגם הלא מצופה, בעקבות התוספת של ציפוי הNb לעובי הדגם האפקטיבי ובגלל זרמי המיסוך הנוספים שזורמים בו, התורמים שניהם ליציבות הדגם שם. כמו כן, התמונות המגנטו-אופטיות מראות כי ציפוי הNb עוצר בחדות ובאופן מוחלט מפולות שטף הנוצרות באזור הלא מצופה ומתקדמות לגבול עם האזור המצופה, עד שגודל השדה המגנטי וקצב עליית השדה עולים מעל ערכי סף מתאימים, הגבוהים מערכי הסף של הדנדריטים הנוצרים על שפות הדגם החיצוניות. מעל ערכי סף אלו, זרמי המיסוך של שכבת הNb כבר לא מצליחים לעצור את כניסת הדנדריטים מהאזור הלא מצופה, והם אכן נכנסים גם אל האזור המצופה. עבור קצבי עליית שדה מהירים, כל שדות הסף שצוינו כאן קטנים, אי היציבות המגנטית של הדגם גדלה, ויותר מפולות שטף דנדריטיות נכנסות אל אזורי הדגם השונים.

מתוך השוואה של שיטות הציפוי השונות, אנחנו רואים, באופן די מפתיע, כי ציפוי הדגם בשכבת מוליך על נוספת מספק מיסוך יעיל יותר כנגד מפולות השטף הדנדריטיות מאשר ציפוי המתכת, גם בקצבי עליית שדה מהירים; שדות הסף של הדגם מצופה הNb גבוהים משמעותית משדות הסף של הדגם מצופה הנחושת. המשמעות היא שזרמי הMeissner שבשכבת הציפוי של מוליך העל והתרומה שלו לעיבוי הדגם עוצרים בצורה חזקה יותר את התקדמות מפולות השטף מאשר הבלימה האלקטרומגנטית שזרמי הeddy שבציפוי המתכת מפעילים.

מכיוון שכניסת שטף מגנטי (יציבה או לא יציבה) אל דגמים מוליכי על היברידיים, המצופים חלקית בשכבת מוליך על נוספת כמעט ולא נחקרה, אנחנו מקדישים חלק נכבד מעבודה זו לכך וחוקרים גם את השפעתם של שדות מגנטיים איטיים על התנהגות מפולות השטף שבדגם. מתוך תוצאות המדידות המקיפות הללו, אנחנו מציגים ראיות ניסיוניות ראשונות לקיומם של 2 סוגי דנדריטים חדשים וייחודיים: מפולות דנדריטיות היברידיות, הנמצאות בשתי השכבות מוליכות העל שבדגם, והמושפעות משתיהן. ומפולות דנדריטיות משטחיות, הנוצרות רק בשכבת הציפוי, ולא בשכבת מוליך העל התחתונה. לכל אחד מסוגי המפולות החדשות הללו יש התנהגות ומאפיינים הייחודיים לו, הבאים לידי ביטוי בצורה המרחבית השונה שלהם ובתלות שלהם בטמפרטורה; המפולות ההיברידיות הן בעלות צורה דנדריטית מרחבית המושפעת גם מציפוי הNb וגם משכבת הNbN ובעלות תלות חלשה בטמפרטורה. לעומת זאת, המפולות המשטחיות הן בעלות תלות חזקה יותר בטמפרטורה, מכיוון ששכבת הNb בה הן נוצרות בעלת טמפרטורה קריטית נמוכה מזו של שכבת הNbN, ולכן היא רגישה יותר לשינויים קטנים בטמפרטורה.

עבודה זו נעשתה בהדרכתו של פרופסור יוסף ישורון.

המחלקה לפיזיקה של אוניברסיטת בר-אילן.

אוניברסיטת בר אילן

מפולות שטף דנדריטיות במבנים מוליכי-על היברידיים תחת שדות מגנטיים בקצב עלייה גבוה

מיכל וסרמן

עבודה זו מוגשת כחלק מהדרישות לשם קבלת תואר מוסמך
במחלקה לפיזיקה, אוניברסיטת בר אילן

רמת גן התשפ״ג